NANO · MICRO small
www.small-journal.com

Plasmonic Hydrogen Sensors

Bin Ai, Yujing Sun, and Yiping Zhao*

Hydrogen is regarded as the ultimate fuel and energy carrier with a high theoretical energy density and universality of sourcing. However, hydrogen is easy to leak and has a wide flammability range in air. For safely handling hydrogen, robust sensors are in high demand. Plasmonic hydrogen sensors (PHS) are attracting growing interest due to the advantages of high sensitivity, fast response speed, miniaturization, and high-degree of integration, etc. In this review, the mechanism and recent development (mainly after the year 2015) of hydrogen sensors based on plasmonic nanostructures are presented. The working principle of PHS is introduced. The sensing properties and the effects of resonance mode, configuration, material, and structure of the plasmonic nanostructures on the sensing performances are discussed. The merit and demerit of different types of plasmonic nanostructures are summarized and potential development directions are proposed. The aim of this review is not only to clarify the current strategies for PHS, but also to give a comprehensive understanding of the working principle of PHS, which may inspire more ingenious designs and execution of plasmonics for advanced hydrogen sensors.

1. Introduction

Hydrogen, which has the molecular formula H_2, is the gas with the smallest density (0.0899 g L^{-1}) and is required for many essential chemical processes. It also has the potential to be an energy carrier due to its high gravimetric energy density, sustainability, and lack of carbon emissions upon consumption.[1–5] However, significant challenges remain for the safe deployment of H_2 fuel sources, therefore limiting its widespread adoption.[6] The storage and use of H_2 pose unique challenges due to its ease of leaking, low-energy ignition, wide range of combustible fuel-air mixtures, buoyancy, and its ability to embrittle metals. Because H_2 gas has the highest rating on the flammability scale, ignition can occur at a volumetric ratio of H_2 to air as low as 4%. As H_2 generation and H_2 fuel cell technologies continue to be developed, the demand for H_2 sensors for safely handling H_2 gas in all stages of the hydrogen-based economy will rise.[2,3] Thus, reliable H_2 sensors with good stability, high sensitivity, rapid response time, large dynamic range, cost efficiency, and spark-free operation are highly desirable.[2] **Table 1** lists the performance requests for the advanced H_2 sensor.[7]

Various methods for H_2 detection, including catalytic, electrochemical, resistive, mechanical, and optical measurements have been investigated, as listed in **Table 2**.[8–10] In particular, resistive H_2 sensors are currently the most studied category in literature and well commercialized. Metal-oxides are the major materials used for resistive H_2 sensors. Recently, low-dimensional materials, such as graphene oxide and carbon nanotube, have been studied and achieved remarkable hydrogen sensing performances.[11,12] However, the electronics-based H_2 sensors, including catalytic, electro-chemical, and resistive in Table 2, have been extensively studied and commercialized. Such sensors rely on probing the electrical signal changes of a responsive material exposed to H_2 gas.[13] Serious concerns about the safe operation are raised due to possible sparking caused by applied voltage in the flammable H_2 environment.[13] Recently, there has been a growing interest in optical H_2 sensors because they can effectively avoid the danger of explosion in the combustible gas environment by separating the optical sensing part from the electronic processing part. Moreover, optical hydrogen sensors show a series of advances, such as high resistance to electromagnetic (EM) interference, large sensitivity, remote measurement, and miniaturization.[14–17] The most common optical hydrogen sensors are based on optical fibers, including Bragg grating and tapered single-mode fiber.[18–23] Hydrogen is detected by the changes in the optical properties caused by changes in the dielectric properties of metals after they become hydrides. Optical hydrogen sensors based on interferometry and gastrochromism are also developed.[24–26] However, these optical hydrogen sensors show some problems, such as reduction in mechanical strength on the fabrication process, temperature compensation in practical applications, complicated operation, high cost, and large size. Recently, nanostructured hydrogen sensors based on surface plasmon (SP) resonance (SPR) and their derivative phenomena began to appear, termed

B. Ai, Y. Sun
School of Microelectronics and Communication Engineering
Chongqing University
Chongqing 400044, P. R. China
E-mail: binai@uga.edu
B. Ai
Chongqing Key Laboratory of Bio perception & Intelligent Information Processing
Chongqing 400044, P. R. China
Y. Zhao
Department of Physics and Astronomy
University of Georgia
Athens, GA 30602, USA
The ORCID identification number(s) for the author(s) of this article can be found under https://doi.org/10.1002/smll.202107882.

DOI: 10.1002/smll.202107882

Table 1. Typical performance requirements for hydrogen sensors in stationary and automotive applications.[7]

	Stationary	Automotive
Measuring range	Up to 4 vol.% H_2 (survive 100%)	
Lower detection limit (LOD)	< 0.1 vol. %	
Response time (t_{90})	< 30 s	< 1 s
Recovery time (t_{10})	< 30 s	< 1 s
Accuracy	±10%	±5%
Ambient temperature	−20 to +50 °C	−40 to +125 °C
Ambient pressure	80–110 kPa	62–107 kPa
Ambient relative humidity	20–80%	0–100%
Lifetime	> 5 years	

as plasmonic hydrogen sensors (PHS), showing great potential in high-performance devices. A series of advances have been demonstrated for PHSs, such as high sensitivity, fast response speed, miniaturization, and high-degree of integration, which are difficult to achieve or cannot be realized by traditional sensing methods.

Systematical summaries, particularly regarding PHSs, are rare with the exception of Langhammer's short review in the year 2015.[13] When we prepared this review, Langhammer published an impressive perspective on nanostructured Pd-based hydrogen sensors,[27] which emphasized their limitation for commercial uses. In this context, we present the mechanism and recent development of PHS (from the year 2015 to 2021), aiming to give a comprehensive understanding of the working principle of PHSs, follow up on the developing trends of PHSs, and inspire innovative ideas for the development of high-performance hydrogen sensors. This review consists of two major sections: the mechanism and the discussion of previous works. In the mechanism section, the basics of the plasmonic effect as well as thermodynamics and kinetics of metal hydride during hydrogenation and dehydrogenation are presented. Then, the sensing principle of the PHSs is introduced. In the summary of previous works, the PHSs are cataloged into nanoparticle (NP)-based and plasmonic film-based PHSs according to the structure and plasmonic effect. The effects of the configuration, geometry, and materials of the plasmonic nanostructures on sensing performance for each type of PHS are summarized. Finally, the future avenues and challenges for hydrogen sensors based on plasmonic nanostructures are discussed.

2. Mechanism

2.1. Plasmonic Effect

The plasmonic effect is induced by SPR which are coherent oscillations of conduction electrons at a metal-dielectric interface film excited by external EM radiation. SPR exists on the surface of a metal and has two different modes according to the microscopic morphology of the metal: local surface plasmon resonance (LSPR) and surface plasmon polariton (SPP). The response of SPR to the change of the dielectric environment in the vicinity of the metal surface and/or the variation of the permittivity of the metal itself forms the basis of plasmonic sensors.

LSPR is excited in a confined metallic structure such as NPs when the incident photon frequency is in resonance with the collective oscillation of the conduction electrons (**Figure 1**a). When the dimension of NPs is much smaller than the light wavelength λ, the extinction $E(\lambda)$ of a spherical metallic NP, which is the sum of absorption and scattering cross sections, is given by the following equation according to the "quasi-static theory",[33]

$$E(\lambda) \propto \left[\frac{\varepsilon_i}{\left(\varepsilon_r + \chi \varepsilon_d\right)^2 + \varepsilon_i^2} \right] \tag{1}$$

where ε_d is the dielectric constant of the surrounding medium, λ is the excitation wavelength, χ is a shape factor that describes the NP's aspect ratio ($\chi = 2$ for a sphere and is proportional to the aspect ratio of the NP), and ε_r and ε_i are the real and

Table 2. Characteristics of different hydrogen sensors.

Sensors type	Operating principle/ device	Functional material	Advantages	Disadvantages
Catalytic[28]	Pellistor	Pt, Pt, Al_2O_3, SnO_2,	Stability, wide temperature range, long life	Poor selectivity, easy to poison, slow response speed, oxygen dependence, unsafe operation
Electro-chemical[29]	Amperometric	Pt, sulfuric Acid, Nafion, Teflon PTFE	High sensitivity, low energy consumption, no heating, poisoning resistance, adapt to high temperature	Narrow temperature range, needs electrolyte, not resistant to aging, calibration cycle, cross sensitivity, high cost, unsafe operation
Resistive[30]	Semiconducting metal–oxide	SnO_2, ZnO, TiO_2, FeO, Fe_2O_3, NiO, Ga_2O_3, In_2O_3, Sb_2O_5, MoO_3, and WO_3	High sensitivity, fast response, acceptable lifetime, wide operating temperature range, low cost, modest power consumption	Poor selectivity, susceptible to interference, high temperature conditions, pollution, aging and memory effects, oxygen dependence, unsafe operation
Mechanical[31]	Cantilever	Pt, Pd	Micromachinable, small size, no fire source in explosive environment, independent of oxygen	Slow response, easy to poison, ages easily
Optical[32]	Optrode	Pd, WO_3, MoO_3, Y	No ignition source, wide area monitoring, independent of oxygen, free from electromagnetic interference	Interference from ambient light, drift due to aging effects, easy to poison

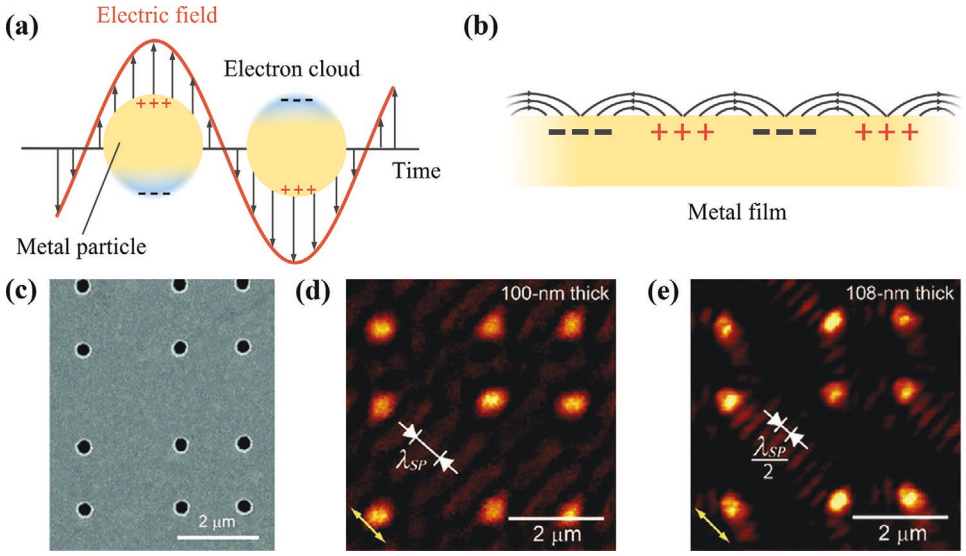

Figure 1. Schematics of a) LSPR and b) SPP. c) SEM image of an Au nanohole array with diameter and period of 250 nm and 2 μm, respectively. d) Near-field image of the nanohole array in a 100 nm thick gold film. White arrows denote the wavelength of the fringes, which is equal to the SP wavelength (λ_{SP}). e) Near-field image of the nanohole array in a 108 nm thick gold film. White arrows denote the wavelength of the fringes, which is equal to half of the SP wavelength ($\lambda_{SP}/2$). Yellow arrows indicate the polarization direction of incident light. Reproduced with permission.[34] Copyright 2006, American Chemical Society.

imaginary parts of the dielectric function of the metal, $\varepsilon_m = \varepsilon_r + i\varepsilon_i$, respectively. When $|\varepsilon_r| \gg \varepsilon_i$, the LSPR occurs when $E(\lambda)$ has a maximum, that is, $\varepsilon_i(\lambda_0) \approx -\chi\varepsilon_d$. The resonance wavelength λ_0 is determined by ε_d and redshifts with an increase in ε_d due to the buildup of polarization charges on the dielectric side of the interface. For nonspherical metal NPs, the shape factor is different for different polarizations of the incident EM wave, manifesting in a shape dependence of the LSPR extinction spectra. For larger metal NPs beyond the Rayleigh approximation (diameter $d > 30$ nm), the dipolar resonance redshifts and suffers a substantial broadening.

SPPs can be excited by the coupling between an EM wave and a SP at a metal–dielectric interface (Figure 1b). The propagation constant of a SP (k_{sp}) at a metal-dielectric interface can be expressed as,

$$k_{sp} = \frac{2\pi}{\lambda}\sqrt{\frac{\varepsilon_d\varepsilon_m}{\varepsilon_d + \varepsilon_m}} \tag{2}$$

SPP cannot be created on a smooth metal surface wave by direct optical excitation because the k_{sp} is always smaller than $\frac{2\pi}{\lambda}$, the propagation constant of an EM wave in the free space, that is, the direct light-to-SP conversion is forbidden. Therefore, special coupling schemes, mainly prism coupler, waveguide coupler, and grating coupler, are used, and the corresponding exciton conditions are

$$\frac{2\pi}{\lambda} n_p \sin\theta = \mathrm{Re}\{k_{sp}\}(\mathrm{prism}) \tag{3}$$

$$k_{mode} = \mathrm{Re}\{k_{sp}\}(\mathrm{waveguide}) \tag{4}$$

$$\frac{2\pi}{\lambda} n_d \sin\theta + m\frac{2\pi}{a_0} = \mathrm{Re}\{k_{sp}\}(\mathrm{grating}) \tag{5}$$

where n_p is the refractive index (RI) of the prism, k_{mode} is the propagation constant of the waveguide mode, n_d is the RI of the surrounding medium, m is an integer and denotes the diffraction order, and a_0 is the period of a grating.

Other than the external coupler, multiple SPR models can be excited by the structured metal films, which are termed plasmonic films. For example, the optical properties of nanohole array films[34,35] are determined by both LSPR and SPP effects as shown in Figure 1c–e.[34] In Figure 1d,e captured by near-field scanning optical microscopy (NSOM), the bright hot spots indicate the LSPR effect while the fringes are caused by SPP, respectively. SPP can propagate tens to hundreds of micrometers along the metal surface. The long propagation distance and coupling between LSPR and SPP can significantly improve the sensitivity of plasmonic films.

Overall, the plasmonic films have the characteristics of high stability, easy integration, convenient use, and large sensitivity.

2.2. Metal-Hydrogen Interaction

All H_2 sensors consist of an active material, which in most cases is a metal hydride or metal alloy hydride. The particular metal, metal alloy, or compound can change their crystal and chemical structures upon H_2 immersion under the appropriate conditions, thus changing their optical properties. Therefore, it is important to understand the hydrogenation/dehydrogenation process and their property changes.

2.2.1. Thermodynamics

Many metals, intermetallic compounds, and alloys can react with hydrogen to form solid metal hydrides. The phase

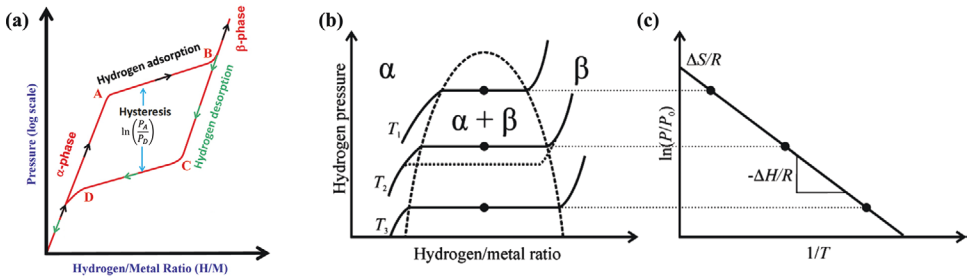

Figure 2. a) Typical pressure-composition curves for the hydrogenation and dehydrogenation of a metal hydride under a fixed temperature *T*. Reproduced with permission.[39] Copyright 2014, Wiley. b) Pressure-composition-temperature curves for the hydrogenation of a metal hydride under different *T* ($T_1 > T_2 > T_3$). c) A typical van't Hoff plot of a metal hydride. Reproduced with permission.[13] Copyright 2014, American Chemical Society.

transition from metal-to-metal hydrides (dielectric) leads to a significant permittivity change. Understanding the metal-hydrogen interaction in the hydrogenation and dehydrogenation process is the basis of the PHSs. The hydrogenation and dehydrogenation are the mutual reverse processes for a metal hydride, and following the reaction,

$$M + \frac{x}{2}\mathrm{H_2} \leftrightarrow \mathrm{MH}_x + Q \tag{6}$$

where Q is the heat of hydride formation. However, the hydrogenation and dehydrogenation processes are not totally reversible. The hydrogenation is exothermic, while the dehydrogenation is endothermic. **Figure 2** shows a typical pressure-composition-temperature (P-C-T) curve during a hydrogenation and dehydrogenation cycle. Hydrogen molecules dissociate on the metal surface and enter the metal lattice (forming α-phase) under the increasing hydrogen pressure P_H. The mixed states of hydrogen and crystal lattice change from the α-phase (mixed-phase) with low hydrogen atom density to a saturated β-phase when the P_H reaches location "A" in Figure 2a.[36,37] The P_H almost remains constant while the hydrogen content increases significantly, forms a plateau, and ends at location "B". The plateau pressure followed the van't Hoff relation,[38]

$$\mathrm{In}P_H = \frac{\Delta H}{RT} - \frac{\Delta S}{R} \tag{7}$$

where ΔH and ΔS are the enthalpy and entropy of hydride formation or decomposition, R is the universal gas constant, and T is the temperature. Clearly, the plateau pressure will decrease with temperature, indicating that metal hydrides are easier to be formed at higher temperatures. Figure 2b shows the hydrogenation process at different temperatures ($T_1 > T_2 > T_3$). The plateau (mixed-phase) becomes short as T increases. The heat of formation can be extracted by plotting the plateau pressure $\ln(P/P_0)$ versus $1/T$ (van 't Hoff plot) (Figure 2c), where ΔH and ΔS can be obtained by the slope of the line and its intersection with the y-axis, respectively. The dehydrogenation process is a reverse process with a desorption plateau (Figure 2), with a lower P_H (location "C" to location "D" as compared to the hydrogenation plateau). The hydrogenation and dehydrogenation processes form a hysteresis loop. The free energy difference associated with the hysteresis is determined by,

$$\Delta G_{\mathrm{hyst}} = \mathrm{RT}\ln\left(\frac{P_A}{P_D}\right) \tag{8}$$

where P_A and P_D are the hydrogen pressures at locations "A" and "D", respectively. The hysteresis represents a loss in the efficiency of the hydride due to irreversible degradation of the material during the hydrogenation/dehydrogenation processes. A good hydride material for an H_2 sensor should have a hysteresis, that is, the width of the plateau, $\Delta(H/M)_r$, as small as possible. Otherwise, a large hysteresis makes the sensor readout no nspecific in the sense that it will not only depend on the current P_H but also on the history of the P_H applied, and it is impossible to unambiguously determine absolute pressures in a continuous fashion.

2.2.2. Kinetics

One of the most important parameters for hydrogen sensors is their response time. Though other sensor design factors could influence this parameter, the response time of the hydrogen sensor is mainly determined by the kinetics of the active material. The hydrogenation process involves several steps that can be described by the Lennard-Jones potential as shown in **Figure 3**a.[40,41] When a hydrogen molecule approaches the metal surface, it is first physiosorbed on the surface due to van der Waals forces or electrostatic attraction. When the pressure and temperature are high enough, an electron can be transferred between the metal and the hydrogen, leading to the dissociation of the hydrogen molecule. The hydrogen atoms move to subsurface sites, rapidly diffuse through the material, and form a solution of H in the metal, that is, the α-phase as shown in Figure 2. At this stage, the hydrogen molecule is chemisorbed in the metal. Then, the α-phase is transformed to the β-phase with increasing hydrogen concentration. Such a phase transition is usually accompanied by a crystalline structure change and a volume expansion, thus inducing other physical property changes.

Specifically, for a metal particle, the hydrogenation process experienced four stages as shown in Figure 3b:[39,42] 1) Hydrogen adsorption. The hydrogen will be physiosorbed on the metal surface and prepared to diffuse into the metal; 2) Hydride nucleation. Hydrogen will start to react with the metal to form metal hydride at the appropriate temperature and pressure. Random hydride patches will be formed on the metal surface, similar to a nucleation process; 3) Hydrogen coalescence. The hydride patches will coalesce and form a hydride shell around a metal

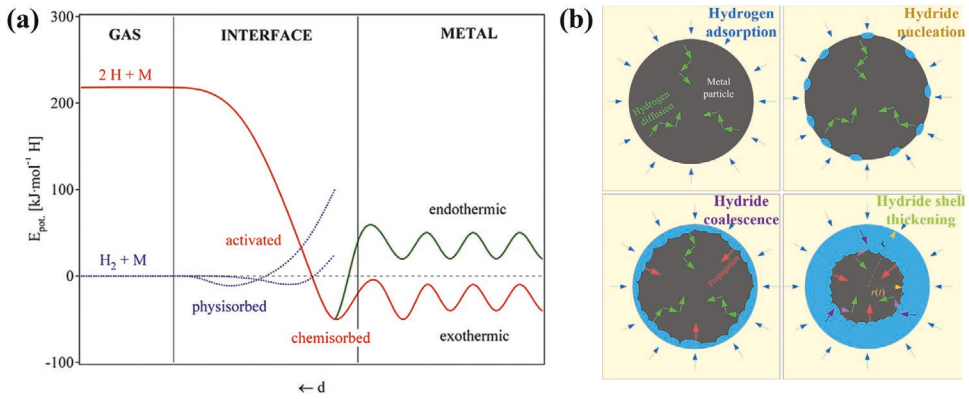

Figure 3. a) Potential energy curve for hydrogen binding to a metal surface: physisorption for both activated and nonactivated processes; dissociation and surface chemisorption; surface penetration and chemisorption on subsurface sites; and diffusion. Reproduced with permission.[41] Copyright 2003, Elsevier. b) Illustration of the four stages of the hydrogenation process for a metal powder. Reproduced with permission.[39] Copyright 2014, Wiley.

particle; 4) Hydride shell thickening. Subsequent metal-hydrogen reactions will involve propagation of the hydride shell, increasing the hydride thickness. These four stages may vary depending on the structure and thickness of the hydride. For example, if the hydride layer is extremely thin, only the first three stages would occur, which could significantly shorten the response time.

For most practical cases, the volume fraction α of a hydride at time t can be fit by Avrami's model,[43]

$$\alpha = 1 - \exp\left(-kt^n\right) \tag{9}$$

where k is treated as the apparent reaction constant, and n depends on the geometry and dimensionality of the reaction. The reaction rate k is thermally activated and follows the Arrhenius relation,

$$k = k_0 \exp\left(-\frac{E_a}{k_B T}\right) \tag{10}$$

where E_a is the reaction activation energy, and k_B is the Boltzmann constant. The activation energy for hydrogenation and dehydrogenation may be different for the same metal/metal hydride, depending on the structure, morphology, and catalyst used. To lower the activation energy, catalysts can be added to the metal-metal hydride systems.

During the hydrogenation/dehydrogenation process, the optical property/permittivity would change significantly. **Figure 4** shows the permittivity of two typical hydrogen-active metals (Pd and Mg) before, during, and after hydrogenation.[44] Upon hydrogenation, these metals present different characteristics: Pd becomes distinctly less metallic at a fairly uniform rate with the real part ε_r increasing by up to 39% in the near-infrared wavelength region, and the imaginary part ε_i decreasing by a similar percentage; the ε_m of Mg changes dramatically, from a metal to an insulator, and the maximum change in its ε_r occurs at the wavelength of 1.5 µm. The change of permittivity during the hydrogenation/dehydrogenation process would lead to variation in plasmon resonance wavelength and spectrum intensity according to Equations (3)–(6), which are the primary mechanisms for PHS.

2.3. Working Principle of PHSs

There are two different PHS sensing configurations: direct and indirect hydrogen detections.[13] Taking NPs, for example, in the

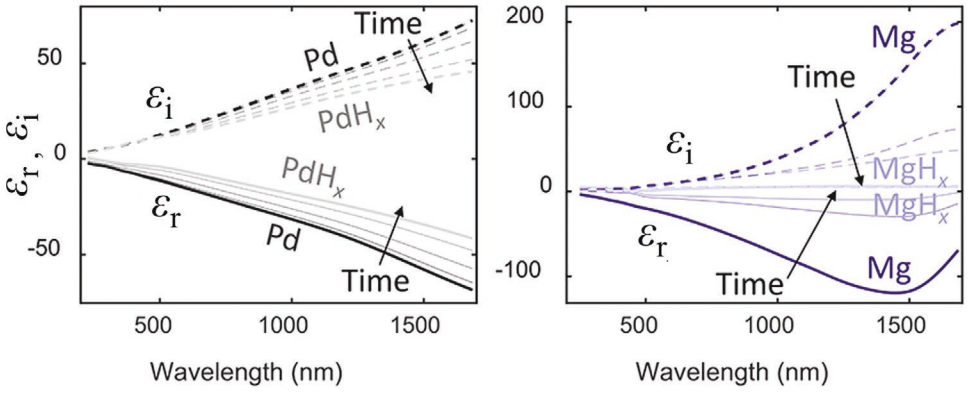

Figure 4. Dielectric functions of Pd and Mg, their hydrides, and the intermediate loading states. ε_r is shown as solid lines and ε_i as dashed lines. The arrows indicate the hydrogenation time. As time progresses, the shading of the lines gets lighter. Reproduced with permission.[44] Copyright 2018, American Chemical Society.

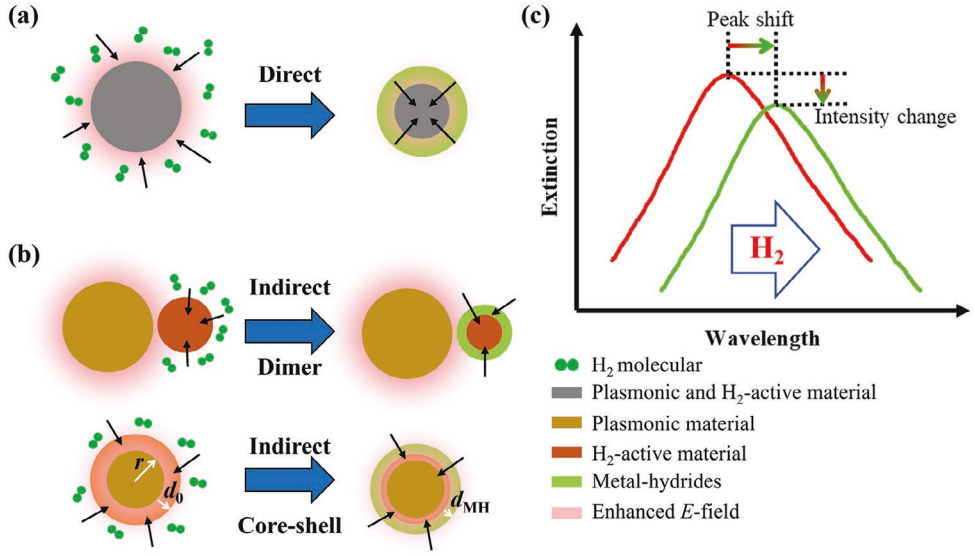

Figure 5. Schematics of the a) direct and b) indirect sensing systems. The indirect PHSs consist of dimer, core-shell, and two-layer configurations. c) The change of extinction spectra $E(\lambda)$ of a plasmonic NP induced by hydrogen exposure for the direct and indirect sensing cases.

direct detection configuration (**Figure 5**a), nanostructures of materials such as Pd act both as the active and plasmonic material, reacting with hydrogen, forming hydrides, and producing transducer signals. The indirect sensing configuration usually consists of a nanostructure with an inert plasmonic material such as Au, Ag, or Al, coated by an active material, such as Pd, Y, TiO_2, CeO_2, etc., forming core-shell, dimer, or two-layer configuration (Figure 5b). Hydrogen would react with the active material, leading to a change in the RI, which is then probed by the plasmonic materials. The hydrogenation process for both direct and indirect PHSs follows the four stages as discussed in Figure 3b. Also, during the hydrogenation/dehydrogenation processes, both the volume expansion and the change in RI will shift the plasmonic resonances. Therefore, hydrogen can be detected by tracking the change of resonance wavelength and intensity before and after the exposure of hydrogen (Figure 5c). Basically, indirect detection was better than direct detection which is based on single metal, because indirect detection usually has two or more materials that can possess both strong SPR and large hydrogen adsorption. However, direct detection based on alloys is beyond indirect detection due to the fact that alloys have stronger interaction between different materials and are easier to prepare than the nanostructures used for indirect detection.

A simple estimation of the change of LSPR wavelength $\Delta\lambda_p$ during the hydrogenation process for a core-shell configuration is proposed below. As shown in Figure 5b, the spherical core with a radius of r is a plasmonic particle that will not be hydrogenated, while the shell with a thickness of d_0 is the active sensing layer and can be hydrogenated. Assuming that at a fixed H_2 partial pressure P_H, temperature T, and a detection duration t, a volume fraction α of the shell is hydrogenated so that the effective shell thickness is changed to d_{MH}. Assuming that the shell is thin enough so that the hydride nucleation will occur across the entire metal layer, then according to the molecular sensing mechanism of a spherical LSPR NP, $\Delta\lambda_p$ is given by,[45,46]

$$\Delta\lambda_p = s\left[n_{MH}(\alpha) - n_M\right] + sn_0\left(e^{-\frac{2d_{MH}}{\delta}} - e^{-\frac{2d_0}{\delta}}\right) - s\left[n_{MH}(\alpha)e^{-\frac{2d_{MH}}{\delta}} - n_M e^{-\frac{2d_0}{\delta}}\right] \quad (11)$$

where n_{MH}, n_M, and n_0 are the effective RI of metal-hydride with a hydride volume fraction α, the RI of the metal, and the RI of the surrounding medium, respectively; s is the sensitivity of the LSPR NP and δ is the effective length of the local electric field of the plasmonic NP. In addition, assuming that after the metal is fully hydrogenated, there is a constant volume expansion, $V_{MH} = (1 + \xi)\, V_M$, where ξ is the volume expansion coefficient $\xi > 0$. For the shell, the original metal volume is $V_M = 4\pi r^2 d_0$, and after partial hydrogenation, the volume changes to $V_{MH}(\alpha) = (1 - \alpha)\, V_M + (1 + \xi)\alpha\, V_M = 4\pi r^2 d_{MH}$. Thus $d_{MH} = (1 + \alpha\xi)d_0$. If α is sufficiently small ($\ll 1$), according to Maxwell–Gannet effective medium theory,[47] $\varepsilon_{MH}(\alpha) \approx \varepsilon_M + \alpha(\varepsilon_{MH} - \varepsilon_M)$, and $n_{MH}(\alpha) = \sqrt{\varepsilon_{MH}(\alpha)} = \sqrt{\varepsilon_M}\left(1 + \frac{\alpha}{2}\frac{\varepsilon_{MH} - \varepsilon_M}{\varepsilon_M}\right)$. Therefore, Equation (11) can be written as,

$$\Delta\lambda_p = s\frac{\alpha}{2}\frac{\varepsilon_{MH} - \varepsilon_M}{\sqrt{\varepsilon_M}}\left(1 - e^{-\frac{2d_0}{\delta}}\right) + s\frac{\alpha\xi d_0}{\delta}e^{-\frac{2d_0}{\delta}}\left(\sqrt{\varepsilon_M} - n_0\right) + s\frac{\alpha^2}{2}\frac{\varepsilon_{MH} - \varepsilon_M}{\sqrt{\varepsilon_M}}\frac{\xi d_0}{\delta}e^{-\frac{2d_0}{\delta}} \quad (12)$$

Equation (12) shows that the change in $\Delta\lambda_p$ is very complicated, depending on the hydrogenation mechanism and the dielectric function change, as well as volume expansion. If the shell layer is totally hydrogenated, Equation (11) changes to

$$\Delta\lambda_p = s(n_{MH} - n_M) + sn_0 e^{-\frac{d_0}{\delta}}(n_M - 1) + se^{-\frac{(1+\xi)d_0}{\delta}}(n_0 - n_{MH}) \quad (13)$$

Equation (13) determines the maximum $\Delta\lambda$ shift, that is, the dynamic range of the sensor. Clearly, for a real PHS design, Equations (11)–(13) are oversimplified. They do not consider that both ε_m and ε_{MH} are complex, and that their responses to H_2 are varying depending on wavelength as shown in Figure 4. In addition, the kinetics is also complicated. The primary working principle for SPP-based structured films is the same as that of the LSPR-based NPs, also including direct and indirect hydrogen detections. The calculation of the hydrogen sensing performances of SPP-based structured film has not been figured out now. So far, a systematic and detailed study on the PHS sensing mechanism has not been presented in the literature.

3. Discussion of Previous Works

Below, we will introduce recent developments in PHS. SPP-based PHSs (Kretschmann configuration) have been extensively discussed in previous reviews,[8] and are not the focus of this review. We group the PHS into NP-based and plasmonic film-based PHSs, which are based on LSPR and LSPR/SPP mechanisms, respectively. Other strategies to improve hydrogen detection performances are introduced in a separate section. **Table 3** gives an overview of plasmonic configurations and materials used in the literature, and the corresponding detailed sensing performances are summarized in **Table 4**. The

Table 3. Overview of the plasmonic structures in literature.

		Configuration	Materials	Mechanism	Ref.
Plasmonic NPs	Direct Hydrogen Detection	 Pure Metal	Au, Pd, Y, Zr, Ti, V	Hydrogenation directly detected by LSPR	[44,48–58]
		 Alloys	PdAu, PdAg, PdCu, PdAuCu		[59–67]
	Indirect Hydrogen Detection	 Dimer	Pd-Au	Hydrogenation detected in LSPR enhanced area	[59,68–71]
		 Stacked NP			[72]
		 Core-shell	Pd-Au, Au-CeO_2, and Au-CdC		[73–77]
Plasmonic Films	Direct Hydrogen Detection	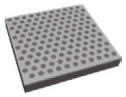 Nanohole Array Film	Pd	Hydrogenation directly detected by SPP and LSPR	[78–82]
		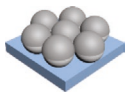 Nanoshell Array Film	Pd, PdAu, PdAg, and PdCo		[83]
	Indirect Hydrogen Detection	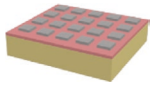 MIM	Pd-Au	Hydrogenation detected by LSPR coupled with SPP	[84–89]
Other Improvement Strategies	Surface modification	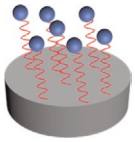	Pd modified by CTAB, TOAB, CTAC, and PVP	Changes metal surface property	[90]
	Polymer coating	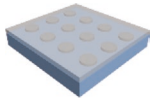	Pd coated by PMMA and Teflon AF; AuPd coated by PTFE and PMMA	Protects metal and diffusion property of H_2 in the polymer	[91,92]

Table 4. Sensing metrics and mechanism of state-of-art PHSs at room-temperature.

Model	Structures	Size	t_{90}*	LOD*	Studied Hydrogen Range	Hysteresis-free?	Mechanism	Ref.
Plasmonic NPs	Au NPs	Diameter = 60 nm	A few seconds	0.5%	0–5%	N.A.	Photothermal response induced by plasmonic resonances	[48]
	Au NPs	Diameter = 10–50 nm	0.3–1 s (4%)	N.A.	0–4%	N.A.	Hot electron induced H_2 dissociation and the subsequent formation of a metastable gold hydride (AuH_x)	[49]
	Pd strips on butterfly wings	Length = 200 um Width = 50–120 nm Thickness = 15 nm	20 s (1 mbar)	10 ppm	0.1–4%	No	Coupling between plasmonic model of Pd NPs and optical resonant mode of the Morpho biophotonic architectures	[50]
	Pd NPs in Teflon AF	Diameter = 8–11 nm	5 s (100 mbar)	30 ppm	0–250 mbar	No	Polymer protection; Amorphous polymer for fast diffusion of H_2	[51]
	Y nanorods	With = 160 nm Length = 385 nm Height = 50 nm	50 s (5%)	N.A.	0–5% in N_2	N.A.	Phase transition from metallic yttrium dihydride (YH_2) to the insulating trihydride (YH_3) upon hydrogen exposure	[52]
	PdAu alloy nanodisks 25% Au	Diameter = 67 nm Height = 15 nm	< 1 s (40 mbar)	N.A.	1 mbar–1 bar	Yes	Combine strong LSPR and low hysteresis of Au with strong H_2 adsorption of Pd	[63]
	PdAu alloy nanodisks on fiber 25% Au***	Diameter = 170 nm Thickness = 25 nm	40 s (40 mbar)	N.A.	≈3 mbar–300 mbar	No	Combines strong LSPR and low hysteresis of Au with strong H_2 adsorption of Pd	[60]
	PdAuCu alloy nanodisks	Diameter = 190 nm Thickness = 25 nm	0.4 s (40 mbar)	1- 5 ubar in pure hydrogen 5 ppm in Ar 40–50 ppm in synthetic air	5 ppm–100%	Yes	Combines Pd, Au, and Cu	[61]
	AuPd nanospirals	Wire radius = 13 nm Helix radius = 25 nm Pitch = 130 nm	< 20 s (0–2.5%)	N.A.	0–2.5% in N_2	Yes	Chiral response; AuPd alloy	[93]
Plasmonic Films	Pd bilayer lattices	Lattice constant = 500 nm Hole and NP diameter = 385 nm Thickness = 40 nm	55 s (1 mbar)	N.A.	1 mbar–1 bar	No	Coupling of SPP and LSPR between the bilayers	[82]
	PdCo alloy hemisphere film	Diameter = 500 nm Thickness = 5 nm	≤ 0.15 s (40 mbar) 0.85 s (1 mbar)	2.5 ppm	1 mbar–1 bar	Yes	Alloys; Coupling of SPP and LSPR of the hemisphere film	[94]
Other Improvement Strategies	PdAu alloy nanodisks in PTFE 30% Au	Diameter = 100–190 nm Thickness = 25 nm	0.3 s (40 mbar)	1 ppm in Ar 5 ppm in air 5 ubar in pure hydrogen	1 ppm–100%	Yes	Combines strong LSPR and low hysteresis of Au with strong H_2 adsorption of Pd; Protected by PTFE for high resistance	[91]

Notes: *The response time to reach 90% of the total signal limit of detection; **The limit of detection; ***The composition ratio of the alloys in this review is atom ratio, at.% and is simplified as % in this paper. N.A.: not addressed.

details are discussed in the rest of this review according to the sequence listed in Table 3.

3.1. Plasmonic NPs Based Hydrogen Sensors

Plasmonic NPs have been used extensively for LSPR-based hydrogen sensors. Configuration of the NP-based PHSs with different materials, shape, and size determines the hydrogen sensing performance, which leads to two kinds of hydrogen sensors: direct and indirect hydrogen detectors. Their primary working principle is described in Section 2.3.

3.1.1. Direct Hydrogen Detection Based on Plasmonic NPs

Direct hydrogen detection of plasmonic NPs is usually based on metals or metal alloys that have significant changes in

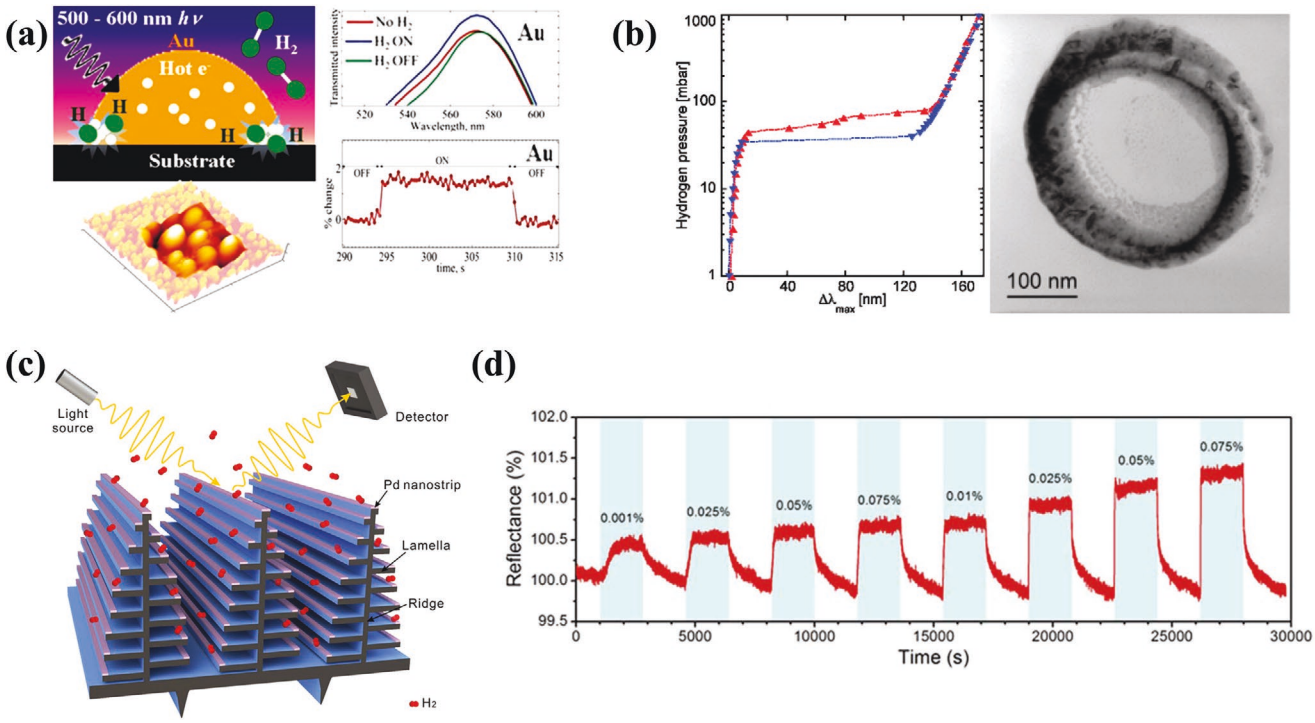

Figure 6. a) Top-left image: schematic of the H_2 dissociation process on Au surface. Bottom-left image: AFM image of the Au NPs. Top-right image: transmission spectra of the Au NPs with/without H_2. Bottom-right image: graph of the real-time monitoring of changes in transmitted intensity with H_2 ON and OFF. Reproduced with permission.[49] Copyright 2014, American Chemical Society. b) Left image: optical hydrogenation isotherms for Pd nanorings with 100-nm wall thickness obtained at 55 °C. Right image: SEM image of a single nanoring with 100-nm wall thickness. The main observations are the appearance of a "double plateau" upon hydrogenation. Reproduced with permission.[54] Copyright 2012, American Chemical Society. c) Schematic illustration showing optical H_2 sensing based on the 3D heterogeneous structures that consist of Pd nanostrips and the photonic architectures of the Morpho butterfly wing scales. d) Normalized reflectance change at wavelength of 500 nm in different H2 concentrations showing a detection limit below 10 ppm. Reproduced with permission.[50] Copyright 2018, The Royal Society of Chemistry.

dielectric function during hydrogeneration or have strong metal-hydrogen interactions. There are two different catalogs: single metal and metal alloy nanostructures.

Single Metal: Plasmonic effect is the primary characteristic of PHSs. A natural strategy is to use metals that can generate strong SPR, such as Au and Ag NPs, for hydrogen detection. However, the most commonly used plasmonic metals such as Au and Ag, do not form stable hydride structures and are not good sensing materials for H_2. Recently Sil et al. found that Au could lead to H_2 dissociation by hot electron and subsequent formation of a metastable gold hydride (AuH_x) (**Figure 6**a).[49] This effect led the Au nano-hemispheres to show ≈1.8% increase in the transmitted intensity for 4% H_2 in 0.3–1 s, demonstrating the ability to use Au for direct hydrogen detection. Li et al. reported an H_2 sensor based on photothermal response around a single Au NP.[48] Heat is induced by the plasmonic resonance of the Au NP and then transferred to the surrounding gas environment, leading to the detection of 0–5% H_2 with the LOD of 0.5% in Ar. In contrast, to the best of our knowledge, there is no report on using Ag for direct hydrogen sensing, which may be due to the fact that Ag cannot uptake any H_2 as well as its unstable surface properties. The mechanism of using traditional plasmonic metals (Au and Ag) to probe H_2 is based on their strong plasmonic resonances, while the sensitivity (signal change) is typically low because their adsorption of H_2 is weak, and the change of RI is small. To improve the sensitivity, the metals for PHSs should possess both considerable plasmonic effect and hydrogen-metal interaction.

Pd has been proven to be a good candidate because it supports good hydrogen absorption under normal temperature and pressure (Figure 4a), while still possessing considerable plasmonic properties.[95,96] Langhammer et al. first used Pd nanodisks for direct LSPR sensors in 2007.[53] Pressure-LSPR-response isotherms were observed and obeyed Sievert's law in the low-pressure range, exhibiting a characteristic "plateau" at 18 Torr upon hydrogen charging and 7.5 Torr upon hydrogen discharging. The plateau pressure was found to increase with temperature.[53,58] The absolute hydrogen concentration could be calculated from the LSPR signal based on a proposed linear dependence of the LSPR response to hydrogen uptake.[97,98] Pd nanorings lead to asymmetric hysteresis (Figure 6b) due to the influence of the H_2 and defect-induced tensile strains present in their inhomogeneous structure combined with specifics of the hydrogenation/dehydrogenation kinetics.[54] He et al. fabricated Pd nanostrips on butterfly wings (Figure 6c).[50] The hydrogen sensing performance could be enhanced by the coupling of the plasmonic mode of the Pd nanostrips with the optical resonant mode of the Morpho biophotonic architectures, generating a sharp reflectance peak and achieving a LOD = 10 ppm (Figure 6d) and t_{90} = 20 s for 0.1% H_2. Combining the above results and mechanism studies,[55,56] the hydrogen-Pd

interaction shows the following characteristics: 1) hydride formation enthalpy and entropy are nearly independent of individual Pd NP size or shape; 2) the hysteresis of the hydrogenation process of nanostructured Pd is significantly wider than that in bulk, and details depend on the specific structure of the NPs; 3) the absorption behavior of the hysteresis loop is size-dependent in the sub-30 nm regime, whereas desorption is size- and shape-independent; 4) the size and type of grain boundaries and hydride-formation pressure are related, but for dehydrogenation such a direct relationship is absent. The differences between the hydrogenation and dehydrogenation in Pd suggest that the two processes have a different phase-transition pathway. In addition, absorbing hydrogen alters the relative stability of Pd NPs, in favor of icosahedron-based morphologies.[57] Although Pd has achieved larger sensitivity than Au and Ag, whose mechanisms have also been well studied, problems of narrow response pressure range, hysteresis, non-linear responses, susceptibility to temperature, and slow dynamics still exist.[99–102] These problems will decrease the accuracy and make the response time > 10s. In addition, Pd is expensive (≈88 \$ g^{-1}), undermining its commercial applications.

Alternatively, other metals with weak plasmonic response but active hydride formation have been studied for direct hydrogen sensing. Strohfeldt et al. fabricated Yttrium (Y) nanorods with width, length, and height of 160, 385, and 50 nm, respectively.[52] Since the phase of Y can transform from metallic yttrium dihydride (YH_2) to the insulating trihydride (YH_3), the pronounced plasmonic resonance (distinct peak in extinction spectra) generated by YH_2 nanorods would vanish completely when the composition changed to YH_3 during hydrogenation. The authors showed that at λ = 1580 nm, the extinction can change by 300% for absorption/decomposition of 5% H_2 in N_2.[52] However, the response time is large ($t_{90} \approx 50$ s), and the Y surface suffered from the easy adsorption of CO_2 and H_2O in air. The hydrogenations of Zr, Ti, and V have been studied theoretically.[44] Among the three metals, Zr shows the smallest change in optical properties. The real part of the dielectric function of Zr exhibits a very small change during the hydrogenation process, but the imaginary part increases significantly. After hydrogenation of Ti, the TiH_x appears to become more metallic, characterized by a decrease in the real part and an increase in the imaginary parts of the dielectric function with wavelength. Upon hydrogenation, V has a small change in the real part of the dielectric function but a much more significant change in the imaginary part (increasing by more than 38% in the near-infrared region). Thus, Zr has the smallest differential response because of its small change in optical properties upon hydrogenation. The response is in the same order as Ti, with its maximum responses spanning a wider range of wavelengths (from the ultraviolet to the near-infrared) than that of the other two materials. Compared to Pd, Zr, Ti, and V all have a much smaller change in optical response, which is expected to cause lower sensitivity. The performances may be enhanced and meet the request in specific applications as more efforts are made on these metals and others.

Another promising metal is Mg, which has long been recognized as a very promising material for hydrogen storage,[103,104] and has shown a larger change of refractive index than that of Pd (Figure 4) during hydrogenation. In addition, Mg is quite cheap (≈ 0.3\$ g^{-1}), which is very attractive for PHS development. We believe that Mg deserves more attention in hydrogen sensors. However, there are few reports on using Mg for PHSs. Reasons may be tied to the fact that pure Mg is not chemically stable in air (easy to be oxidized), has a long hydrogenation/dehydrogenation time, and processes a relatively weak plasmonic response.

Single metal-based PHSs work well when P_H is raised over a certain threshold (corresponding to the hydride formation pressure). However, for a detection requiring a large dynamic range and real-time readout, single metal-based PHSs are not suitable for a number of reasons. First, they typically feature a large response in a very limited H_2 pressure range (0–5% in mixed gas, or 0–300 mbar, see Table 4), that is, around the hydride formation pressure (the "plateau"). In other words, their response to the change of P_H is usually nonlinear and strongly dependent on the absolute pressure. Second, pure metal hydride usually has a large hysteresis upon hydride formation and decomposition. This makes the sensor readout nonspecific since it will depend not only on the current P_H but also on the history of the P_H. Hence, it is not possible to unambiguously determine the absolute pressure readout in a continuous fashion. Last, the hydrogenation/dehydrogenation process for a single metal is usually slow, governed by intrinsic chemical reaction barriers, and results in long response times, that is, t_{90} is in the range of a few seconds to 1 min (see Table 4). Overall, the PHSs based on single metals face difficulties in meeting the performance requests of commercial applications as summarized in Table 1.

Alloys: A good LSPR-based hydrogen sensing material should meet two basic requirements: 1) high intrinsic plasmonic response and 2) high intrinsic hydrogenation performance. As discussed before, among pure metals, Au and Ag have high intrinsic plasmonic responses but they either cannot be hydrogenated or show very little H_2-adsorption-related response. However, metals with good hydrogenation behavior, such as Pd, Y, Ti, and Mg, do not have a good plasmonic response. It is very hard to find a pure metal that meets both requirements. Therefore, an alternative strategy is to create a mixed phase of two metallic materials: one with high plasmonic performance, and the other with excellent hydrogenation behavior.

Based on previous discussions, the alloying between the hydride-forming metals (e.g., Pd) with classic plasmonic metals (e.g., Au, Ag) is a natural choice. It is expected that the H_2 sensitivity of the alloyed nanostructures can be enhanced compared to that of the corresponding single metal nanostructures. In addition, Au and Ag can reduce or inhibit the nucleation of the hydride phase, thus cutting down the negative influence of plateau and hysteresis on the sensor readout. Langhammer's group fabricated a series of AuPd alloyed nanodisks with different compositions using successive deposition of alloy element layers through a nanofabricated mask, followed by thermal annealing to promote alloy formation.[63] They found that during hydrogenation the signal change, such as extinction and wavelength shift, became smaller for a large P_H range (1–1000 mbar) when the composition ratio of Au increased. However, in a low P_H range (1–10 mbar), the signal change was in a positive relationship with the composition ratio of Au. The hysteresis was shown to weaken with more Au. When the atomic ratio

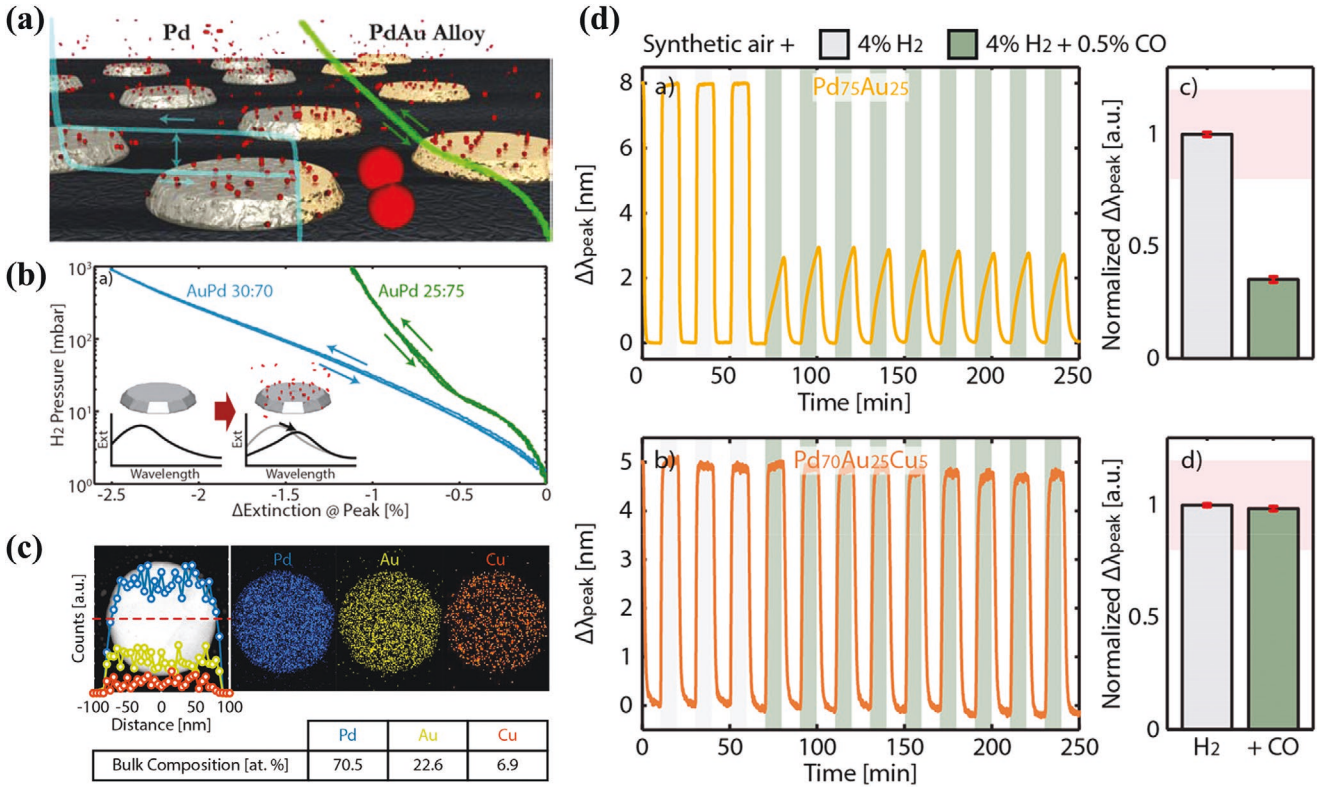

Figure 7. a) Schematics of the Pd and PdAu alloy disks, and their H_2 absorption and desorption isotherms. Reproduced with permission.[63] Copyright 2015, American Chemical Society. b) H_2 absorption and desorption isotherms of 30:70 (blue) and 25:75 (green) AuPd binary alloy systems. Inset: Change of the alloy plasmonic peak resonance upon H_2 absorption. Reproduced with permission.[64] Copyright 2016, American Chemical Society. c) Top-left: STEM image of a single $Pd_{70}Au_{25}Cu_5$ nanodisk together with EDS elemental line-scans along the corresponding red dashed line. Top-right: EDS elemental maps of the nanodisk corroborating the homogeneous nature of the alloy. Bottom: Table containing the elemental composition of the $Pd_{70}Au_{25}Cu_5$ alloy NP, as derived from the EDS analysis. d) $\Delta\lambda_{peak}$ responses of $Pd_{75}Au_{25}$ and $Pd_{70}Au_{25}Cu_{54}$ to 4% H_2 and 4% H_2 + 0.5% CO. Reproduced with permission.[61] Copyright 2019, American Chemical Society.

of Au increased to 25%, the hydrogenation/dehydrogenation induced hysteresis could be negligible, leading to 5% improvement in reading accuracy in the P_H range of 1–1000 mbar (**Figure 7**a), while the absolute sensitivity under low P_H increased 8 times compared to that of the pure Pd sensor. The t_{90} was shortened to be less than 1 s in the P_H range of 0–40 mbar. In addition, they also showed that smaller dimensions could improve the response time. The AuPd nanodisks could be transferred to optical fibers, creating a hysteresis-free fiber PHS.[60] They further reported that the AuPd nanodisks with a 30 (Au):70 (Pd) composition ratio had a better monotonic response to hydrogen in the P_H range of 1–1000 mbar compared to that of the AuPd nanodisks with 25 (Au):75 (Pd) composition ratio (Figure 7b).[64] The total extinction change from AuPd nanodisks with 30:70 ratio was 2.5-fold higher than that of the AuPd nanodisks with 25:75 ratio. Matuschek et al. reported that a Pd-Au alloy chiral nanostructure-based PHS using circular dichroism (CD) spectroscopy could significantly improve response time, linearity, and accuracy.[93] In the report, AuPd nanospirals with Au composition ratio from 0 to 42% were prepared by glancing angle deposition (GLAD). Due to the chirality of the plasmonic helix, a strong CD response (dip-peak-feature) of up to 1.7° was observed, which corresponded to the resonance position of the Pd nanohelix. When the Au content increased, the hysteresis due to hydrogenation/dehydrogenation decreased significantly, and the CD signal increased with the hydrogen concentration in a linear fashion. Additionally, for samples with 23% and 42% Au, the response time in the hydrogenation process was less than 20 s, while the response time of the dehydrogenation process was less than 80 s. Overall, AuPd alloys show significantly enhanced performances in sensitivity, response rate, and hysteresis reduction, and are not resistant to poisoning and deactivation.[105,106]

Ag and Cu have also been reported to alloy with Pd for PHS. Wang et al. investigated PdAg alloy nanosheets for sensitive assessment of the hydrogen evolution reaction (HER) in colloid solutions.[65] The PdAg nanoplates with an Ag-to-Pd ratio of ≈2.1 had a hexagonal shape with a mean diameter of 47.9 ± 4.6 nm (diagonal of the hexagon) and a thickness of ≈5.7 nm. The photocatalytically generated hydrogen reacts with the PdAg nanosheets, resulting in a gradual redshift of LSPR peaks, which appeared to be almost linearly proportional to the amount of hydrogen generated in a volume range of 5 to 35 µL. Regrettably, the response time, sensitivity, and hysteresis of this type of PHS were not reported. Darmadi et al. fabricated CuPd alloyed nanodisks with the Cu ratio from 0 to 30%.[61] As the Cu content increased, the hysteresis reduced until it completely disappeared for $Pd_{70}Cu_{30}$. The PdCu alloy with as little as 5%

Cu showed strong resistance to CO poisoning and sensor deactivation. However, the $\Delta\lambda_p$ and sensitivity decreased from ≈ 25 to ≈ 4 nm and 0.34 to 0.08 nm mbar$^{-0.5}$ as Cu ratio increased. The reduced sensitivity stems from the repulsive Cu-H pair interactions, as well as from the Pd host lattice contraction induced by the addition of Cu due to its smaller atomic radius (i.e., α_{Pd} = 3.89 Å, α_{Cu} = 3.61 Å). They further found that the minimum Cu content required to provide deactivation protection in the 500 ppm CO background in synthetic air was 10%. The required minimum amount of Cu depended on the CO concentration in the background, and a higher CO concentration required a higher Cu content.[66] Clearly, these works show that the AuPd alloys can significantly improve the performance of the PHS, while the CuPd alloy can improve the resistance to poisoning and deactivation.

The above works have suggested that a ternary alloy of Au, Cu, and Pd could not only improve the sensor performance, but also increase their reliability. Darmadi et al. introduced a $Pd_{70}Au_{25}Cu_5$ ternary alloy nanodisk PHS (Figure 7c) and showed that the sensor had i) a limit of detection (LOD) in the ppm range, ii) hysteresis-free response over 5 orders of P_H, iii) subsecond response time at room temperature, iv) CO, CO_2 and CH_4 poisoning resistance in synthetic air (Figure 7d), and v) excellent stability over time.[61] Altogether these performance parameters met or even exceeded the corresponding strict hydrogen sensor performance targets (Table 1). Furthermore, they found that in fact the $Pd_{65}Au_{25}Cu_{10}$ alloy had the best compromise in terms of hysteresis-free response, sensitivity, and CO deactivation resistance.[66] This system also exhibited long-term stability during operation under severe CO poisoning conditions, and no sign of deactivation after more than 50 H_2 pulses and more than 12 h in a 500 ppm CO background.

Langhammer's group summarized the universal scaling and design rules of hydrogen-induced optical properties in Pd and Pd-alloy NPs:[67] 1) the wavelength shift of the plasmonic optical response of hydride-forming Pd or Pd alloy NPs to hydrogen (i.e., the sensitivity defined as $\Delta\lambda_p$/[H/Pd]) is defined solely by the spectral LSPR wavelength of the NPs in the non-hydrogenated state. In other words, the sensitivity will be higher if the initial LSPR wavelength is larger; 2) for particles of similar dimension, to a first-order approximation the sensitivity is a constant and is independent of the composition of the alloy (at least up to 25% as demonstrated here).

3.1.2. Indirect Hydrogen Detection Based on Plasmonic NPs

Indirect hydrogen detection is mainly based on hybrid nanostructures normally consisting of two nanostructures either with a small gap (such as oligomer (Table 3) or dimers (**Figure 8**a)) or stacked with each other (or, generally speaking, multilayered structures such as stacked NPs (Figure 8c) or core-shell NPs (Figure 8d)). One structure is made of a classic plasmonic metal (Au or Ag) and the other of a strong hydrogen absorption metal/material (Pd or other alloys).[107] As discussed in Section 2.3, the change in the dielectric function of the surrounding materials (due to hydrogenation/dehydrogenation) around a plasmonic nanostructure can introduce a change in the optical response of the combined structure. In fact, the sensing response is caused by the change of the EM field coupling of these two nanostructures during the hydrogenation/dehydrogenation. For the gapped structure, each individual nanostructure can be treated as an electric dipole moment. Due to the small gap, the dipole-dipole interaction can significantly

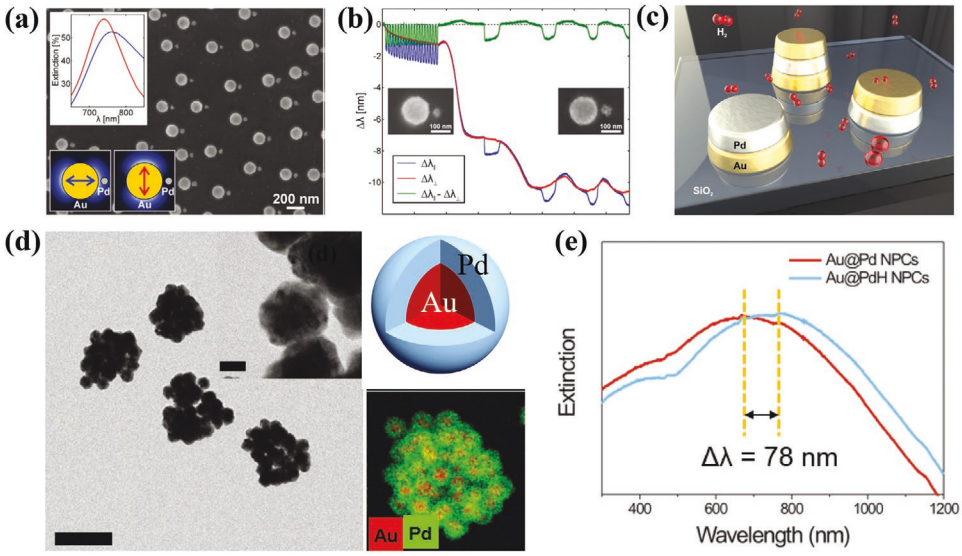

Figure 8. a) Sketch of the drift-corrected nanoplasmonic hydrogen sensing principle with an SEM image of the used AuPd heterodimer structures in the background. b) Graph showing the LSPR-peak response of the sensor for light polarization parallel to the dimer axis (blue), polarization perpendicular to the dimer axis (red), and the difference between the two (green). The correction for long-term irreversible peak shifts in the drift-corrected (green) signal is almost perfect. Reproduced with permission.[59] Copyright 2015, The Royal Society of Chemistry. c) Schematic view of the different stacked Pd-Au nanodisk systems. Reproduced with permission.[72] Copyright 2015, The Optical Society. d) Left image: TEM image of Au@Pd NPC (average Pd shell thickness is 4 nm). The scale bar is 20 nm. Top-right image: schematic of the Au@Pd NP. Bottom-right image: EDS elemental mapping image of an Au@Pd NPC. e) LSPR peak shift when Au@Pd NPC is exposed to dissolved H_2. Reproduced with permission.[75] Copyright 2018, Wiley.

change (red-shift) the LSPR wavelength. However, during the hydrogenation/dehydrogenation, the dipole moment of the hydride changes with H_2 contents, which introduces a change in the LSPR property of the plasmonic structure via coupling. For the overlapped structures such as the core-shell structure, the optical property is determined by EM hybridization, where different LSPR modes will be introduced.[108] The change in the hydride layer during hydrogenation/dehydrogenation will change the hybridization strength, therefore shifting the corresponding hybridization modes. The fundamental principle for the indirect detection strategy is similar to that of the alloy strategy discussed in Section 3.1.1. The only difference is that in the indirect detection, both the plasmonic material and the hydrogen responding material are separately constructed into different nanostructures in order to achieve both the plasmonic response and the sensing function; while in the direct detection with alloy nanostructures, the plasmonic material and hydrogen responding materials are mixed to form a single nanostructure.

Although dimer-based PHSs were extensively reported on from 2011–2014,[68–71] the passion for studying this configuration has faded recently, possibly due to the complicated fabrication process and the shift of interest to alloys. The hydrogen sensing performances can be greatly enhanced by the coworking of the strong LSPR, sensitive hydrogen responses, and the plasmonic coupling in the small gap. Recently Wadell et al. reported a new feature of the Au-Pd heterodimer PHSs (Figure 8a), that is, the dimer structure can be used to calibrate the readout shift of the sensor due to the polarization-dependent responses.[59] As shown in Figure 8b, during the hydrogenation/dehydrogenation, the Pd-Au dimers showed strong responses if the polarization of the incident light was parallel to the dimer-axis (blue curve), but no responses when the polarization rotated 90° (red curve). Thus, the perpendicular polarization readout can be used to efficiently correct for the drifts that occur due to the changes in the composition of the sensor or due to nonspecific events such as a temperature change (green curve in Figure 8b). The two readouts from both polarizations could be realized simultaneously using a polarizing beam splitter, and thus be used to continuously correct the sensor response in order to eliminate long-term drift and aging effects.

For the overlapped structures, the order of the plasmonic structure and the hydride each play an important role. Strohfeldt et al. have conducted a systematic study on the influence of stacking order and geometry of the Au(top)/Pd, Pd (top)/Au, and Au/Pd/Au NPs (Figure 8c).[72] Both experimental and numerical results showed that the $\Delta\lambda_p$ in the same hydrogen pressure region (from 0% to 4% hydrogen) strongly depended on the material order: the Au(top)/Pd NPs exhibited the largest shift (34 nm), while the sandwiched Au/Pd/Au NPs had the smallest shift (16 nm). The stacked NPs have not been widely studied. However, compared to the gapped structures, the stacked NPs can be easily fabricated via a single lithography step, enabling straightforward high-throughput processing.

Core-shell NPs can be synthesized by high-throughput chemical methods and are the most studied configuration for indirect PHSs. In the literature, the most reported core-shell structures for PHSs are made of Au and Pd with varied shapes. For example, Au nanobipyramid@Pd NPs showed a redshift $\Delta\lambda_p$ of 140 nm at 2% H_2 in N_2,[74] while Au@Pd nanorods with controlled length showed $\Delta\lambda_p \approx 40$ nm with the exposition to 1% hydrogen gas.[73] Colloidal clusters with aggregated core-shell NPs showed better performance. Wy et al. prepared colloidal clusters of Au@Pd core-shell NPs (Au@Pd NPCs) by growing a Pd shell on Au NPC (Figure 8d) and studied the hydrogen sensing performance in aqueous solution.[75] When Au@Pd NPCs were exposed to dissolved H_2, its LSPR peak shift was $\Delta\lambda_p = 78$ nm (Figure 8e). The sensitivity was much higher than that of the individual Au/Pd NPs ($\Delta\lambda_p = 7$ nm) and the previously reported Au-Pd bimetallic nanostructures. Such an effect can be attributed to highly promoted local electric fields in the gaps of the clusters (hot spots). Furthermore, the system showed good stability during multiple cycles of hydrogen absorption and release. However, there are some drawbacks to using the chemically synthesized core-shell structures for PHSs, as the size and shape of the core-shell NPs cannot be precisely controlled, leading to the low repeatability of the sensing behaviors. They are all formed in solution which limits their H_2 sensing applications. In addition, the specific values of LOD, response time, hysteresis, and stability are rarely reported for these structures.

Such a drawback can be circumvented using plasmonic NP embedded thin films. Carpenter's group reported the H_2 sensing performances of an Au-CeO_2 rough thin film.[76] The composite Au-CeO_2 thin film was fabricated by subsequent deposition of CeO_2, Au, and CeO_2, followed by an annealing process, generating a rough composite film with ≈15 nm Au NPs and showed strong LSPR behavior. The $\Delta\lambda_p$ was 11 nm upon exposure to 5% H_2 and increased to 15 nm for 20% H_2 at 300 °C in the wavelength range of 500–850 nm. The detection range of hydrogen in an oxygen-free atmosphere experiment was 0.38% to 60%.

4. Summary

In a summary, Pd is still the most studied material for direct LSPR-based PHSs, including Pd-based alloyed materials. The sensitivity of Pd PHSs can be improved by engineering Pd NPs into various shapes or through EM coupling effect. However, Pd still has the issues of large hysteresis, slow response rate, and low stability. Pd NPs alloyed with Au and Cu show great potential in solving these problems. Au-based alloys can reduce hysteresis, increase sensitivity, and shorten response time, while Cu-based alloys improve the poisoning resistance and deactivation. The ternary alloy of PdAuCu with optimized composition exhibits the best hydrogen sensing performance. Indirect PHSs with configurations of dimers, stacked NPs, and core-shell NPs also show enhanced sensing performances compared to those of single metal NPs, but their performances are, in general, worse than those of alloyed NPs. Overall, for the LSPR-based PHSs, the alloyed NPs seem to be the best choice. Clearly, Pd alloys other than with Au, Ag, and Cu, or other alloys may result in improvement upon detailed investigation in the future.

Despite the fast development of NP-based PHSs, there are still some challenges. First, Pd is expensive, which significantly prevents wide commercial applications. The alloy materials, such as Au and Y, are also expensive. Thus, from the materials

point of view, future research should give more attention to cheaper materials such as Mg, V, or Cu, and Ag. Second, the most studied NP systems are surface-based structures, which have low density. Such structures have limited optical resonance strength, which tends to produce a weak optical response. Therefore, although NPs are the most studied model for PHSs, the focus is turning toward another plasmonic structure, that is, plasmonic films.

4.1. Plasmonic Film Based Hydrogen Sensors

Plasmonic films are defined as structured films which support both SPP and LSPR. The typical configurations of plasmonic films, including nanohole array films, nanoshell array films, and MIM are summarized in Table 3. Here the SPR-based hydrogen detection, that is, Kretschmann configuration,[109] will not be discussed. The materials for plasmonic films are still mainly Pd and its alloys. The differences in hydrogen detection between plasmonic NP-based and film-based PHSs are expected as the following: 1) The spectra for NP based PHSs normally have one spectral feature, that is, one extinction peak or one reflection dip due to LSPR, while those of plasmonic films have multiple spectral features, including valleys and peaks, due to various mechanisms such as the coupling between LSPR and SPP (Section 2.1), the interference effect, or extraordinary optical transmission (EOT) of nanohole array films.[110] Thus, multiple responses can be obtained during hydrogenation/dehydrogenation; 2) Plasmonic films support both SPP and LSPR, leading to > 100 nm resonance attenuation distance,[111] which is much larger than that of the LSPR for the metallic NPs (≈10 nm). The large resonance attenuation distance and the coupling between LSPR and SPP could make the plasmonic films more sensitive to the change of hydrides; 3) Plasmonic films have a large surface area, which may lead to slower responses. Research efforts on plasmonic film-based PHSs are far fewer than those of NP-based PHSs, because the fabrication of plasmonic films is generally more expensive, complicated, and less efficient. Nevertheless, the plasmonic films have the characteristics of high stability, easy integration, and convenient use. Due to recent advancements in nanofabrication, especially soft lithography techniques,[112,113] research on plasmonic film-based PHSs has begun to attract more attention. These sensors can also be cataloged as direct and indirect hydrogen sensors.

4.1.1. Direct Hydrogen Detection Based on Plasmonic Films

Similar to Section 3.1.1, the materials used for direct H_2 detection should also meet the two conditions discussed: high plasmonic response and high H_2 induced optical response. In the literature, Pd and its alloys are still the most studied materials for plasmonic film-based PHSs, and the sensing principle is similar to that of the NP-based PHSs. More research efforts have been focused on the design of film configurations. So far, two configurations, nanohole array films, and nanoshell array films, have been investigated.

Nanohole Array Films: Nanohole arrays perforated on metal thin films are a well-known system that supports SPP and LSPR, and generates EOT.[110] Maeda et al. fabricated Pd rectangle (0.8 μm × 0.5 μm) nanohole array films with a thickness of 100 nm and a period of 1.1 μm.[78,79] The zero-order transmission spectra of the hole arrays were recorded at normal incidence in the infrared wavelength region 2.5–10 μm, showing a 200 nm peak shift at 2% H_2. This peak shift value is much larger than those of NPs reported in Section 3.1 (usually < 50 nm). This large $\Delta\lambda$ was attributed to the permittivity change and the lattice expansion of the Pd film after hydrogenation. The reduction of the hole width due to the Pd expansion is estimated to be on the order of a few tens of nanometers.[80] However, this structure was fabricated via electron-beam lithography and the optical measurement was conducted by an infrared microscope. Nishijima et al. compared the H_2 sensing performances of Pd nanodisks (diameter ≈0.63–0.77 μm) and Pd nanohole arrays (hole diameter ≈0.53–0.63 μm) with a period of 1.36–1.52 μm at infrared wavelength region (4–8 μm).[81] Both the nanodisks and nanohole arrays showed very similar sensing behavior, that is, the spectral peak shifted 140–160 nm after 40 min exposure to 4% hydrogen. Such a similarity may have been because the structures were too large. Similarly, Luong et al. compared the hydrogen sensing performances of Pd nanohole arrays and Pd NPs with the same diameter (≈ 380 nm) and period (500 nm) (**Figure 9**a) fabricated by an efficient and low-cost colloidal lithography technique in the wavelength range of 400–1000 nm.[82] The $\Delta\lambda$ of Pd nanohole arrays was observed ≈160 nm from when H_2 pressure changed from 1 mbar to 1 bar, while for the Pd NPs under the same condition, the $\Delta\lambda$ was only 80 nm. In addition, the Pd nanohole arrays showed a faster response than Pd NPs at low P_H (Figure 9b). Also, when the Pd NPs overlapped the Pd nanohole array (bilayer nanolattice), such as the right structure in Figure 9a, strong EM coupling between the NPs and nanoholes induced unusual optical properties upon the hydrogen sorption. When considering the relative transmission intensity $\left(\frac{\Delta T(P_{H_2})}{T_{0\,\mathrm{mbar}}} = \frac{T_{P_{H_2}} - T_{0\,\mathrm{mbar}}}{T_{0\,\mathrm{mbar}}}\right)$ as a function of pressure, the bilayer-nano-lattice showed a sensitivity of 10.6%/mbar, which is about 2- and 4-times higher than that of the Pd nanohole array and Pd NP. At a low P_H (< 3 mbar), the response time of the bilayer nano-lattices at the coupling resonance wavelength was about 70 s, which was around 4- and 10- times faster than that of the isolated nanohole array (≈300 s) and NP (≈700 s) sensors (Figure 9b).

Nanoshell Array Films: Luong et al. developed a PHS based on a Pd and Pd-alloy nanoshell array film (Figure 9c).[94] The nanoshells grown on polystyrene spheres with a diameter of 500 nm in fact formed nanohole arrays under the appropriate deposition conditions.[114] The Pd nanoshell array films yielded an extraordinarily rapid response to hydrogen gas (< 3 s at 1 mbar H_2) with weak hysteresis. By incorporating 20% Ag, Au, or Co to form alloys, the sensing performance of the Pd-alloy nanoshell sensors was significantly enhanced. The best performance was reported for the $Pd_{80}Co_{20}$ sensor, with a response time ≈ 0.85 s at 1 mbar of H_2, a LOD of 2.5 ppm in nitrogen, and 10 ppm in air, no hysteresis, and robustness against aging, temperature, moisture, and interfering gases.

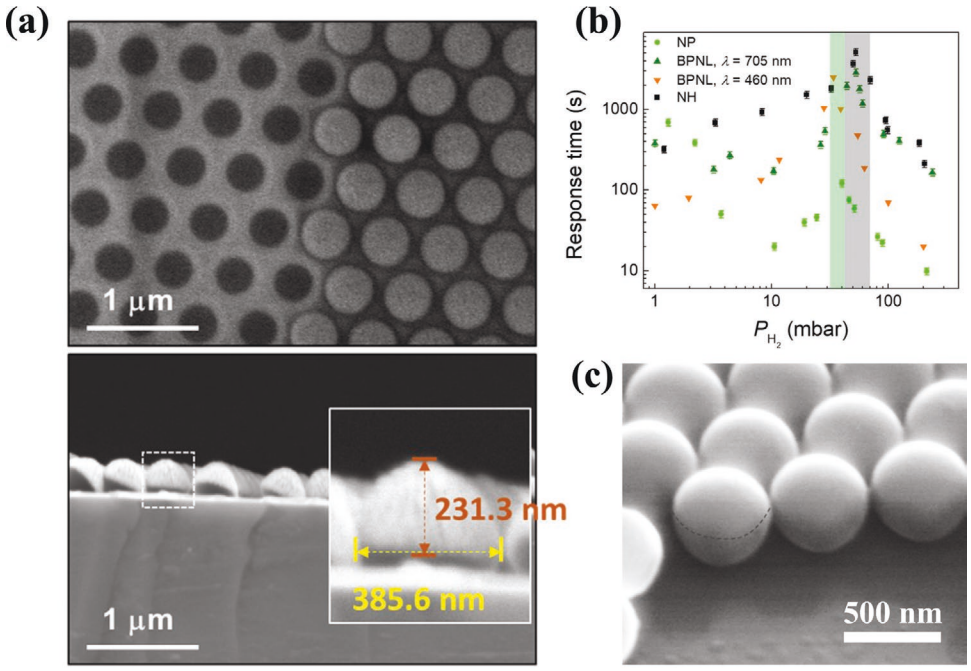

Figure 9. a) Top-view (top) and side-view (bottom) SEM images of the nanohole array, NP, and the bilayer nano-lattice. b) Response times (t_{90}) of nanohole array, NP, and the bilayer nano-lattice (at $\lambda = 460$ and 705 nm). Reproduced with permission.[82] Copyright 2020, Elsevier. c) Side-view SEM image of Pd nanoshell array. Reproduced with permission.[94] Copyright 2021, The authors, The Springer Nature.

4.1.2. Indirect Hydrogen Detection Based on Plasmonic Films

In principle, it would be very hard to design indirect detection structures for the plasmonic thin-film case. The only indirect hydrogen detection for plasmonic films was reported based on the metal-insulator-metal (MIM) configuration (Table 3). The top and bottom metals are normally hydrogen-active metal NPs and plasmonic metal film, respectively. The MIM configuration, consisting of Au NPs/air/Pd film, for hydrogen sensors was first proposed in a numerical calculation paper by Xu et al.[84] Their calculations suggested that the localized electric field in the air gap between the Au NPs and Pd film was strongly enhanced, and any change in the dielectric property of the Pd film would significantly affect the plasmon resonance of the Au NPs, leading to the sensitive response to H_2. The sensitivity was greatly affected by the size and gap of the Au NPs. When the diameter of the NPs and air gap were 70 and 5 nm, respectively, the Au NPs/air/Pd film showed the largest $\Delta\lambda$ of 6.34 nm after Pd became PdH completely. Dhawan's group introduced a MIM PHS composed of Au nanowire grating/Pd film/Au film.[85] Their numerical calculations showed that the change in the dielectric properties of Pd film upon hydrogenation manifested because the incident radiation was coupled into the plasmon waveguide modes in the plasmonic grating, leading to a maximum $\Delta\lambda$ of ≈ 41 nm for $PdH_{x=0.65}$. They further calculated the hydrogen sensing performances of the Pd-coated Au nanogratings and the $\Delta\lambda$ was estimated to be ≈80 nm for $PdH_{x=0.65}$.[86]

The MIM configuration has been widely studied in experiments. A Pd/Y (WO_3)/Au MIM configuration was investigated by Beni et al. (**Figure 10**a,b), and a fast response time of 10 s (Figure 10c) was reported.[87] The working principle of the structure was to induce the coupling between SPP on the Au film and LSPR of the Pd nanodisks and promote enhanced local *E*-fields penetrating into the Y or WO_3 volume. The Y spacer led to a blue resonance shift of ≈300 nm while the WO_3 spacer resulted in a red resonance shift of ≈200 nm upon exposure to 100% H_2. Giessen's group fabricated a Pd nanodisk/MgF_2/Au film structure by laser interference lithography (Figure 10d).[88] The structure provided nearly perfect absorption at $\lambda = 730$ and 950 nm. The change of the absolute reflectance at $\lambda = 950$ nm, from below 1% to above 4% was observed when the H_2 concentration increased from 0 to 4% (Figure 10e), which translates into a relative signal change of almost 400%. The plasmonic coupling of the Pd nanodisks with the other two layers allowed for the confinement of the energy of the incident electric field within the layered structure.[91] The signal change for the MIM structure was larger than that of individual Pd nanodisks because the change of the effective dielectric properties was manifested in the enhanced electric field of the coupling between LSPR and SPP.

In a summary, research on plasmonic film-based PHSs is the subject of increasing attention, and a growing number of impressive works have been reported. The $\Delta\lambda$ for 0% to 100% H_2 was usually higher than 100 nm, which was several times larger than that of NP-based PHSs (usually < 50 nm). The sensitivity of plasmonic film-based PHSs is generally higher than that of NP-based PHSs. Although the response time of plasmonic films may be slower than that of NPs due to the large surface area or volume, the plasmonic film-based PHS could still achieve a fast response time, with one reported value below 0.85 s.[94] This value is faster than most of the NP-based PHSs. Other advantages of plasmonic films have been discussed at the beginning of Section 3.2. However, the reports on plasmonic

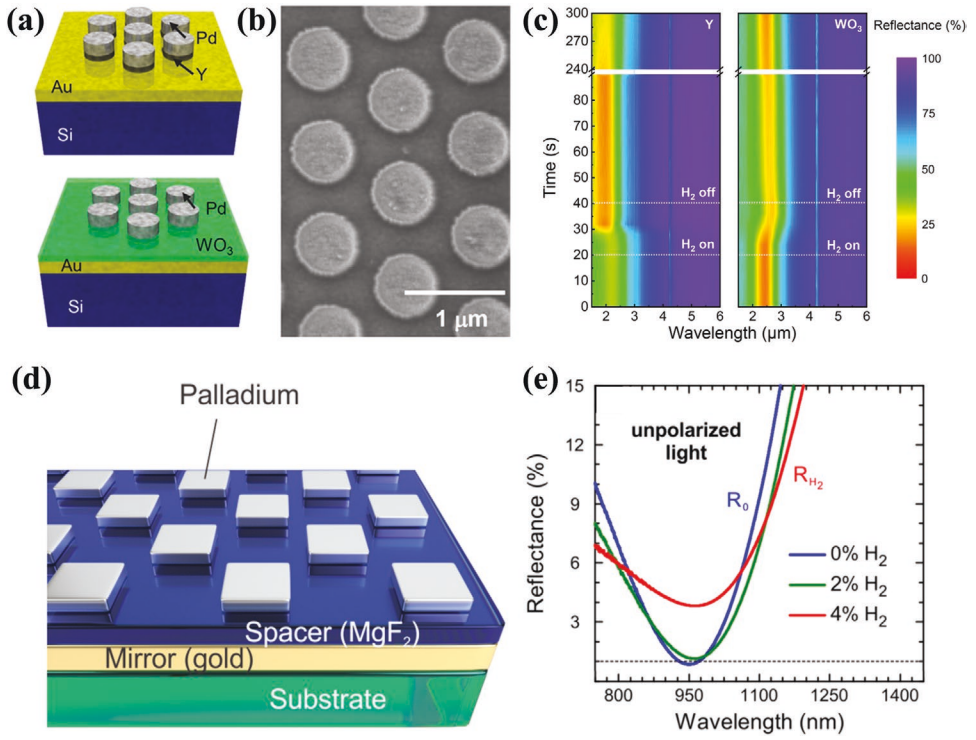

Figure 10. a) Schematic illustration of Pd/Y (WO_3)/Au film. For Y, the layer was only located under the Pd nanodisk, while WO_3 had a uniform film above the Au mirror. b) SEM image of a typical sample with 650 nm diameter and 750 nm period. c) Time dependence of reflection spectra during hydrogenation (on/off) acquired in 4 s intervals. Hydrogen concentration was 100%. Reproduced with permission.[87] Copyright 2019, American Chemical Society. d) Schematic view of the large-area perfect absorber sensor of Pd nanodisk/MgF_2/Au film. e) Reflection measurement of the large-area perfect absorber for different H_2 concentrations in the N_2 carrier gas. The initial reflectance of the sample (blue line) increases after hydrogen exposure (green line, 2%; red line, 4% hydrogen in nitrogen). Reproduced with permission.[88] Copyright 2016, American Chemical Society.

film-based PHSs are very limited so far, and thus, they deserve deeper inspection. For example, the structures reported focused on nanohole, nanoshell, and MIM, which are simple plasmonic models. Complicated nanostructured films with enhanced plasmonic properties, for example, plasmonic films with resonance cavities[115,116] and nanogaps,[117] could be expected to show higher H_2 sensing performances.

4.2. Other Sensor Improvement Strategies

The sensing performances of PHSs can also be significantly altered/improved by other methods. In particular, surface modification and polymer coatings have proven to be effective. Stolaś et al. studied the hydrogen interaction kinetics of surface modification using four surfactants and stabilizers (cetyltrimethylammonium bromide (CTAB), tetraoctylammonium bromide (TOAB), cetyltrimethylammonium chloride (CTAC), and poly(vinylpyrrolidone) (PVP)) on Pd NPs. They found that CTAB, TOAB, and CTAC could significantly decelerate the (de) hydrogenation surface reaction (**Figure 11**a), with the amplitude of deceleration mediated by the halide-ion-Pd surface interaction strength and surfactant surface density.[90] CTAB, TOAB, and CTAC effectively blocked a significant fraction of Pd surface atoms, and reduced the number of available sites for H_2 dissociation or association during absorption and desorption, respectively, thus increasing the response time for complete (de)hydrogenation. However, the polymeric PVP coating could significantly accelerate hydrogen sorption due to the associated reduction of the apparent activation barriers. The surface modification of these four surfactants and stabilizers can protect the Pd surface and enhance the resistance to poisonous gas.

Functional polymers coated on the PHSs are found to have profound effects on the performance of the sensors. Darmadi et al. discovered that when Pd NPs were embedded in poly(methyl methacrylate) (PMMA), high resistance to CO could be achieved. The performance of the sensor was virtually unchanged even after 50 weeks due to the fact that PMMA provided protection against deactivation by CO (Figure 11b).[92] However, due to the PMMA covering, the change in the extinction spectra was not very significant, and the response time became larger due to the slow H_2 diffusion into the polymer matrix. To resolve the slow H_2 diffusion problem, Östergren et al. used amorphous fluorinated polymer poly(4,5-difluoro-2,2-bis(trifluoromethyl)-1,3-dioxole-co-tetrafluoroethylene) (Teflon AF) to embed Pd NPs.[51] Teflon AF displayed a substantially higher H_2 permeability due to a considerably large fraction of free volume, thereby enabling a response time of t_{50} = 2.5 s at 100 mbar H_2, LOD = 30 ppm, and 18 h stability in 4% H_2 in synthetic air (i.e., 100 cycles). Nugroho et al. embedded AuPd (Au:Pd = 30:70) alloy nanodisks in PTFE and PMMA, achieving a LOD of 1 ppm, t_{90} < 1 s, and better resistance to gas interference (Figure 11c) than those of bare alloyed disks.[91] Sensor operation in demanding chemical environments was

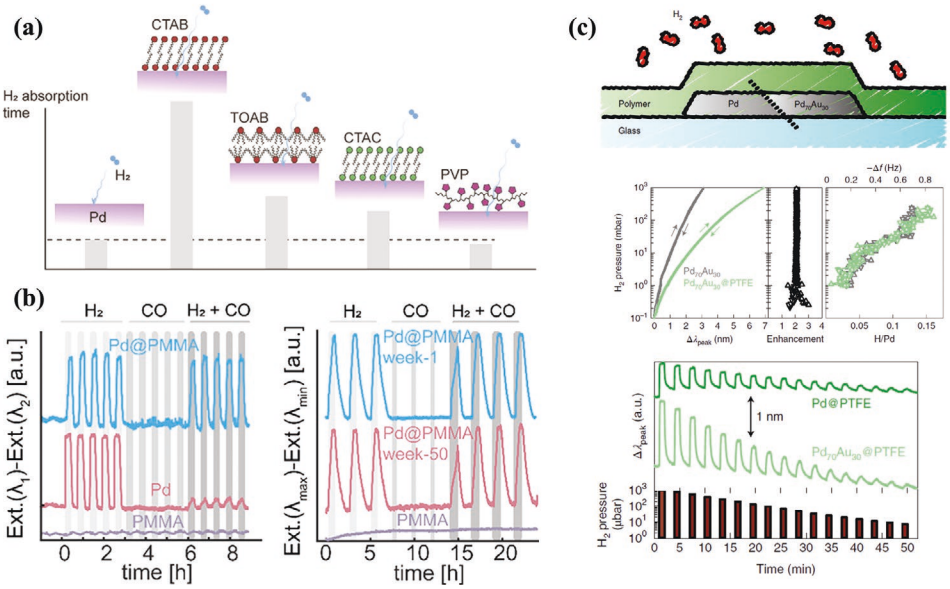

Figure 11. a) H_2 absorption time for the bare Pd NPs and the Pd NPs with CTAB, TOAB, CTAC, and PVP. Reproduced with permission.[90] Copyright 2020, American Chemical Society. b) Left graph: sensor response for the Pd NPs in PMMA, bare Pd NPs without PMMA, and neat PMMA exposed to five subsequent cycles of 10% H_2, five cycles of 0.5% CO, and five cycles of 10% H_2 + 0.5% CO, all in the synthetic air carrier gas. Right graph: fresh and 50 weeks aged Pd NPs in PMMA and neat PMMA sensor cap response to three subsequent cycles of 10% H_2, three cycles of 0.5% CO, and four cycles of 10% H_2 + 0.5% CO, all in the synthetic air carrier gas. Reproduced with permission.[92] Copyright 2020, American Chemical Society. c) Top: schematic of a plasmonic metal-polymer nanomaterial comprising hydride-forming Pd or $Pd_{70}Au_{30}$alloy NPs and a thin polymer coating. Middle: optical absorption/desorption isotherms and pressure-composition isotherms of $Pd_{70}Au_{30}$ alloy disks before and after polytetrafluoroethylene (PTFE) coating. Bottom: $\Delta\lambda_{peak}$ response to stepwise decreasing P_H in the 7–1000 µbar range. Reroduced with permission.[91] Copyright 2019, The Springer Nature.

enabled, without signs of long-term deactivation. Each of these studies suggests that the overall performance of the PHSs, such as stability, sensitivity, and response time, can be improved by using appropriate surface modification or polymer coating with appropriate materials.

5. Conclusion and Outlook

In this review, we have discussed the mechanism and performance of the PHSs that have emerged in recent years. The PHSs are grouped into NP-based and plasmonic film-based PHSs. NP-based PHSs have been studied very extensively, with particles consisting of pure metal, alloy, and multilayered structures or hybrid structures. These sensors usually have a smaller response time but small sensitivity or signal changes due to limited active material volume. There is much less work on the plasmonic film-based PHSs but they have been proven to have higher sensitivities and better stability. These new materials and novel plasmonic structures have pushed the performance of PHSs to a higher level. Performance parameters, such as LOD < 1 ppm, response time < 1 s, and no hysteresis, have been achieved and partially meet the performance requests in Table 1.

Overall, it is clear that the performance of the PHS is superior to almost all the sensors listed in Table 2. Due to its unique advantages, the PHS has the potential to replace the current resistive-based H_2 sensors in the future. However, to design PHSs that meet all the requirements in Table 1, there are still many challenges. First, there are no clear rules to guide the design of the PHSs. As shown in Figure 4, during the hydrogenation/dehydrogenation, both the ε_r and ε_i of the metal or hydride are changing simultaneously. These changes introduce complexities in plasmonic structure design since most plasmonic sensors only consider the change in ε_r (see Equations (11)–(13)). How the changes in both ε_r and ε_i affect the LSPR property of NP based PHSs or the spectral property of film based PHSs are still not fundamentally understood, and it is expected that the response will be strongly dependent on the structure of the PHSs, that is, whether it is NP based or thin film-based, and whether it is from single metal, alloy, composite, or hybrid structures. Other structural parameters such as size, thickness, period, orders of multiple materials, etc. could also significantly influence the performance of the sensors. The second challenge is the active material. So far Pd is still the dominant sensing material, as clearly illustrated in this review. However, according to Figure 4, Mg shows a very remarkable decrease in absolute values of both the real (ε_1) and imaginary (ε_2) dielectric constants upon hydrogenation, compared to the changes in Pd.[44] This is a great opportunity to explore Mg rather than Pd as an active material for PHS. The drawback is that Mg has a slow response time and large activation energy. Nevertheless, if Mg is properly prepared and incorporated with catalysts, these drawbacks can be overcome. He et al. showed that for 2.25% V decorated Mg nanoblade array,[118,119] the hydrogen absorption activation energy can be reduced to 35 kJ mol^{-1} H_2 (compared to 65–81 kJ mol^{-1} H_2 for Mg powder)[120] and desorption activation energy to 65 kJ mol^{-1} H_2 (compared to 120–156 kJ mol^{-1} H_2 for MgH_2 powder).[121] In addition, the current review shows that Pd binary or ternary

alloys can also be used to significantly improve the performance of PHS, but systematic studies on the fabrication and optical properties of these or other alloys are rare. Other than the conventional plasmonic materials (noble metal), new materials, such as degenerate semiconductors,[122–124] emerge for plasmonic sensors and show impressive performances in gas and ion detection. These new plasmonic materials may offer great potential in PHS. The third challenge is to understand the role of surface modification or polymer coating on the performance of PHS. As mentioned in Section 3.3, these surface treatments can significantly alter the CO resistance or H_2 diffusion. A fundamental understanding of how these processes affect the gas reaction dynamics of the active materials, and a systematic investigation of the effect of other polymers are very necessary. The last challenge is a scalable fabrication. For practical applications, large-scale fabrication of the PHS is key to success. In addition to the expensive Pd used in the literature, many of the PHS fabrication methods are not scalable. Therefore, replacing the Pd (or using the minimum amount of Pd) and making the fabrication process more accessible is the last hurdle for advanced PHS development.

Acknowledgements

B.A. and Y.S. were partially supported by National Natural Science Foundation of China (grant nos. 62105043), Natural Science Foundation of Chongqing of China (cstc2020jcyj-msxmX0614), the Fundamental Research Funds for the Central Universities (2021CDJQY-010), and Fund of Key Laboratory of Advanced Materials of Ministry of Education. Y.Z. was partially supported by a National Science Foundation grant under Grant No. ECCS-1808271. The authors thank Mr. Yoong Sheng Phang for proof-reading this manuscript.

Conflict of Interest

The authors declare no conflict of interest.

Keywords

hydrogen sensors, nanostructures, optics, plasmonics

Received: December 19, 2021
Revised: March 19, 2022
Published online:

[1] R. Ramachandran, *Int. J. Hydrogen Energy* **1998**, *23*, 593.
[2] W. J. Buttner, M. B. Post, R. Burgess, C. Rivkin, *Int. J. Hydrogen Energy* **2011**, *36*, 2462.
[3] M. Hirscher, V. A. Yartys, M. Baricco, J. Bellosta Von Colbe, D. Blanchard, R. C. Bowman, D. P. Broom, C. E. Buckley, F. Chang, P. Chen, Y. W. Cho, J.-C. Crivello, F. Cuevas, W. I. F. David, P. E. De Jongh, R. V. Denys, M. Dornheim, M. Felderhoff, Y. Filinchuk, G. E. Froudakis, D. M. Grant, E. M. Gray, B. C. Hauback, T. He, T. D. Humphries, T. R. Jensen, S. Kim, Y. Kojima, M. Latroche, H.-W. Li, et al., *J. Alloys Compd.* **2020**, *827*, 153548.
[4] H. Nazir, N. Muthuswamy, C. Louis, S. Jose, J. Prakash, M. E. M. Buan, C. Flox, S. Chavan, X. Shi, P. Kauranen, T. Kallio, G. Maia, K. Tammeveski, N. Lymperopoulos, E. Carcadea, E. Veziroglu, A. Iranzo, A. M. Kannan, *Int. J. Hydrogen Energy* **2020**, *45*, 282179.
[5] R. Singh, M. Singh, S. Gautam, *Mater. Today: Proc.* **2021**, *46*, 5420.
[6] A. M. Abdalla, S. Hossain, O. B. Nisfindy, A. T. Azad, M. Dawood, A. K. Azad, *Energy Convers. Manage.* **2018**, *165*, 602.
[7] L. Boon-Brett, J. Bousek, G. Black, P. Moretto, P. Castello, T. Hübert, U. Banach, *Int. J. Hydrogen Energy* **2010**, *35*, 373.
[8] T. Hübert, L. Boon-Brett, G. Black, U. Banach, *Sens. Actuators, B* **2011**, *157*, 329.
[9] G. F. Fine, L. M. Cavanagh, A. Afonja, R. Binions, *Sensors* **2010**, *10*, 5469.
[10] H. Gu, Z. Wang, Y. Hu, *Sensors* **2012**, *12*, 5517.
[11] T. K. N. Pham, J. J. Brown, *ChemistrySelect* **2020**, *5*, 7277.
[12] Y. Cheng, B. Ren, K. Xu, I. Jeerapan, H. Chen, Z. Li, J. Z. Ou, *J. Mater. Chem. C* **2021**, *9*, 3026.
[13] C. Wadell, S. Syrenova, C. Langhammer, *ACS Nano* **2014**, *8*, 119250.
[14] R. C. Jorgenson, S. S. Yee, *Sens. Actuators, B* **1993**, *12*, 213.
[15] S. Sekimoto, H. Nakagawa, S. Okazaki, K. Fukuda, S. Asakura, T. Shigemori, S. Takahashi, *Sens. Actuators, B* **2000**, *66*, 142.
[16] J. Villatoro, D. Luna-Moreno, D. Monzón-Hernández, *Sens. Actuators, B* **2005**, *110*, 23.
[17] D. Luna-Moreno, D. Monzón-Hernández, J. Villatoro, G. Badenes, *Sens. Actuators, B* **2007**, *125*.
[18] L. J. Bannenberg, C. Boelsma, K. Asano, H. Schreuders, B. Dam, *J. Phys. Soc. Jpn.* **2020**, *89*, 051003.
[19] S. F. Silva, L. Coelho, O. Frazao, J. L. Santos, F. X. Malcata, *IEEE Sens. J.* **2012**, *12*, 93.
[20] J. Dai, M. Yang, Z. Yang, Z. Li, Y. Wang, G. Wang, Yi Zhang, Z. Zhuang, *Sens. Actuators, B* **2014**, *190*, 657.
[21] M. Fisser, R. A. Badcock, P. D. Teal, S. Janssens, A. Hunze, *J. Lightwave Technol.* **2018**, *36*, 850.
[22] R. Gupta, A. A. Sagade, G. U. Kulkarni, *Int. J. Hydrogen Energy* **2012**, *37*, 9443.
[23] J. Dai, M. Yang, Y. Chen, K. Cao, H. Liao, P. Zhang, *Opt. Express* **2011**, *19*, 6141.
[24] Y. Li, C. Zhao, B. Xu, D. Wang, M. Yang, *Opt. Commun.* **2018**, *414*, 166.
[25] C. Lueng, P. J. Metaxas, M. Sushruth, M. Kostylev, *Int. J. Hydrogen Energy* **2017**, *42*, 3407.
[26] S. S. Kalanur, I.-H. Yoo, H. Seo, *Sens. Actuators, B* **2017**, *247*, 357.
[27] I. Darmadi, F. A. A. Nugroho, C. Langhammer, *ACS Sens.* **2020**, *5*, 3306.
[28] C.-H. Han, D.-W. Hong, I.-J. Kim, J. Gwak, S.-D. Han, K. C. Singh, *Sens. Actuators, B* **2007**, *128*, 320.
[29] M. Sakthivel, *Int. J. Hydrogen Energy* **2008**, *33*, 905.
[30] L. Boon-Brett, J. Bousek, P. Moretto, *Int. J. Hydrogen Energy* **2009**, *34*, 562.
[31] T. Kiefer, A. Salette, L. G. Villanueva, J. Brugger, *J. Micromech. Microeng.* **2010**, *20*, 105019.
[32] M. Ando, *TrAC, Trends Anal. Chem.* **2006**, *25*, 937.
[33] G. Mie, *Ann. Phys.* **1908**, *330*, 377.
[34] H. Gao, J. Henzie, T. W. Odom, *Nano Lett.* **2006**, *6*, 2104.
[35] B. Ai, Y. Yu, H. Möhwald, G. Zhang, B. Yang, *Adv. Colloid Interface Sci.* **2014**, *206*, 5.
[36] F. Lewis, *Int. J. Hydrogen Energy* **1996**, *21*, 461.
[37] T. B. Flanagan, W. A Oates, *J. Less-Common Met.* **1983**, *92*, 131.
[38] J. H. van't Hoff, *Science* **1905**, *22*, 649.
[39] J. Z. Zhang, J. Li, Y. Li, Y. Zhao, *Hydrogen generation, storage, and utilization*, Wiley Online Library, New York **2014**.
[40] L. Schlapbach, A. Züttel, *Nature* **2001**, *414*, 353.
[41] A. Züttel, *Mater. Today* **2003**, *6*, 24.
[42] M. H. Mintz, Y. Zeiri, *J. Alloys Compd.* **1995**, *216*, 159.
[43] M. Avrami, *J. Chem. Phys.* **1939**, *7*, 1103.
[44] K. J. Palm, J. B. Murray, T. C. Narayan, J. N. Munday, *ACS Photonics* **2018**, *5*, 4677.

[45] L. S. Jung, C. T. Campbell, T. M. Chinowsky, M. N. Mar, S. S. Yee, *Langmuir* **1998**, *14*, 5636.
[46] A. J. Haes, R. P. Van Duyne, *J. Am. Chem. Soc.* **2002**, *124*, 105964.
[47] T. C Choy, *Effective Medium Theory: Principles and Applications*, Oxford University Press, New York **1999**.
[48] X. Li, J. Hong, L. Zhang, *ACS Omega* **2020**, *5*, 271640.
[49] D. Sil, K. D. Gilroy, A. Niaux, A. Boulesbaa, S. Neretina, E. Borguet, *ACS Nano* **2014**, *8*, 7755.
[50] J. He, N. S. Villa, Z. Luo, S. An, Q. Shen, P. Tao, C. Song, J. Wu, T. Deng, W. Shang, *RSC Adv.* **2018**, *8*, 323950.
[51] I. Östergren, A. M. Pourrahimi, I. Darmadi, R. Da Silva, A. Stolaś, S. Lerch, B. Berke, M. Guizar-Sicairos, M. Liebi, G. Foli, V. Palermo, M. Minelli, K. Moth-Poulsen, C. Langhammer, C. Müller, *ACS Appl. Mater. Interfaces* **2021**, *13*, 217242.
[52] N. Strohfeldt, A. Tittl, M. Schäferling, F. Neubrech, U. Kreibig, R. Griessen, H. Giessen, *Nano Lett.* **2014**, *14*, 1140.
[53] C. Langhammer, I. Zorić, B. Kasemo, B. M. Clemens, *Nano Lett.* **2007**, *7*, 3122.
[54] C. Langhammer, E. M. Larsson, V. P. Zhdanov, I. Zorić, *J. Phys. Chem. C* **2012**, *116*, 212017.
[55] S. Syrenova, C. Wadell, F. A. A. Nugroho, T. A. Gschneidtner, Y. A. Diaz Fernandez, G. Nalin, D. Świtlik, F. Westerlund, T. J. Antosiewicz, V. P. Zhdanov, K. Moth-Poulsen, C. Langhammer, *Nat. Mater.* **2015**, *14*, 1236.
[56] S. Alekseeva, A. B. D. S. Fanta, B. Iandolo, T. J. Antosiewicz, F. A. A. Nugroho, J. B. Wagner, A. Burrows, V. P. Zhdanov, C. Langhammer, *Nat. Commun.* **2017**, *8*, 1084.
[57] L. Cusinato, A. Hellman, *J. Phys. Chem. C* **2019**, *123*, 186099.
[58] I. Zorić, E. M. Larsson, B. Kasemo, C. Langhammer, *Adv. Mater.* **2010**, *22*, 4628.
[59] C. Wadell, C. Langhammer, *Nanoscale* **2015**, *7*, 109639.
[60] F. A. A. Nugroho, R. Eklund, S. Nilsson, C. Langhammer, *Nanoscale* **2018**, *10*, 205339.
[61] I. Darmadi, F. A. A. Nugroho, S. Kadkhodazadeh, J. B. Wagner, C. Langhammer, *ACS Sens.* **2019**, *4*, 1424.
[62] M. Matuschek, D. P. Singh, H.-H. Jeong, M. Nesterov, T. Weiss, P. Fischer, F. Neubrech, N. Liu, *Small* **2018**, *14*, 1702990.
[63] C. Wadell, F. A. A. Nugroho, E. Lidström, B. Iandolo, J. B. Wagner, C. Langhammer, *Nano Lett.* **2015**, *15*, 3563.
[64] F. A. A. Nugroho, B. Iandolo, J. B. Wagner, C. Langhammer, *ACS Nano* **2016**, *10*, 2871.
[65] M. Wang, P. Wang, J. Zhang, H. Hou, C. Li, Y. Jin, *Nano Res.* **2018**, *11*, 2093.
[66] I. Darmadi, S. Z. Khairunnisa, D. Tomeček, C. Langhammer, *ACS Appl. Nano Mater.* **2021**, *4*, 8716.
[67] F. A. A. Nugroho, I. Darmadi, V. P. Zhdanov, C. Langhammer, *ACS Nano* **2018**, *12*, 9903.
[68] S. Syrenova, C. Wadell, C. Langhammer, *Nano Lett.* **2014**, *14*, 2655.
[69] A. Yang, M. D. Huntington, M. F Cardinal, S. S. Masango, R. P. Van Duyne, T. W. Odom, *ACS Nano* **2014**, *8*, 7639.
[70] T. Shegai, P. Johansson, C. Langhammer, M. Käll, *Nano Lett.* **2012**, *12*, 2464.
[71] N. Liu, M. L. Tang, M. Hentschel, H. Giessen, A. P Alivisatos, *Nat. Mater.* **2011**, *10*, 631.
[72] N. Strohfeldt, J. Zhao, A. Tittl, H. Giessen, *Opt. Mater. Express* **2015**, *5*, 2525.
[73] S. Rodal-Cedeira, V. Montes-García, L. Polavarapu, D. M. Solís, H. Heidari, A. La Porta, M. Angiola, A. Martucci, J. M. Taboada, F. Obelleiro, S. Bals, J. Pérez-Juste, I. Pastoriza-Santos, *Chem. Mater.* **2016**, *28*, 9169.
[74] H. K. Yip, X. Zhu, X. Zhuo, R. Jiang, Z. Yang, J. Wang, *Adv. Opt. Mater.* **2017**, *5*, 1700740.
[75] Y. Wy, S. Lee, D. H. Wi, S. W. Han, *Part. Part. Syst. Charact.* **2018**, *35*, 1700380.
[76] N. M. Houlihan, N. Karker, R. A. Potyrailo, M. A. Carpenter, *ACS Sens.* **2018**, *3*, 2684.
[77] L. Banu, R. A. Potyrailo, M. A. Carpenter, *J. Phys. Chem. C* **2019**, *123*, 179252.
[78] E. Maeda, S. Mikuriya, K. Endo, I. Yamada, A. Suda, J.-J. Delaunay, *Appl. Phys. Lett.* **2009**, *95*, 133504.
[79] E. Maeda, T. Matsuki, I. Yamada, J.-J. Delaunay, *J. Appl. Phys.* **2012**, *111*, 084502.
[80] R. Tsuji, K. Endo, M. Shuzo, I. Yamada, J. J. Delaunay, *J. Micro/Nanolithogr., MEMS, MOEMS* **2009**, *8*, 021140.
[81] Y. Nishijima, A. Balčytis, G. Seniutinas, S. Juodkazis, A. Arakawa, S. Okazaki, R. Petruškevičius, *Sens. Mater.* **2017**, *29*, 1269.
[82] H. M. Luong, M. T. Pham, R. P. Madhogaria, M.-H. Phan, G. K. Larsen, T. D. Nguyen, *Nano Energy* **2020**, *71*, 104558.
[83] H. M. Luong, M. T. Pham, T. Guin, R. P. Madhogaria, M.-H. Phan, G. K. Larsen, T. D. Nguyen, *Nat. Commun.* **2021**, *12*, 2414.
[84] Q. Xu, C. Pan, Y. Chen, *2016 IEEE International Conference on High Voltage Engineering and Application (Ichve)*, Chengdu **2016**.
[85] Y. Sharma, M. Jaiswal, R. Ghosh, A. Dhawan, *Opt. Sens.* **2019**, *11028*, 110282Z.
[86] S. Subramanian, K. Kumar, A. Dhawan, *RSC Adv.* **2020**, *10*, 4137.
[87] T. Beni, N. Yamasaku, T. Kurotsu, N. To, S. Okazaki, T. Arakawa, A. Balčytis, G. Seniutinas, S. Juodkazis, Y. Nishijima, *ACS Sens.* **2019**, *4*, 2389.
[88] S. Bagheri, N. Strohfeldt, F. Sterl, A. Berrier, A. Tittl, H. Giessen, *ACS Sens.* **2016**, *1*, 1148.
[89] T. Teutsch, N. Strohfeldt, F. Sterl, A. Warsewa, E. Herkert, D. Paone, H. Giessen, C. Tarin, *IEEE Sens. J.* **2018**, *18*, 1946.
[90] A. Stolaś, I. Darmadi, F. A. A. Nugroho, K. Moth-Poulsen, C. Langhammer, *ACS Appl. Nano Mater.* **2020**, *3*, 2647.
[91] F. A. A. Nugroho, I. Darmadi, L. Cusinato, A. Susarrey-Arce, H. Schreuders, L. J. Bannenberg, A. B. Da Silva Fanta, S. Kadkhodazadeh, J. B. Wagner, T. J. Antosiewicz, A. Hellman, V. P. Zhdanov, B. Dam, C. Langhammer, *Nat. Mater.* **2019**, *18*, 489.
[92] I. Darmadi, A. Stolaś, I. Östergren, B. Berke, F. A. A. Nugroho, M. Minelli, S. Lerch, I. Tanyeli, A. Lund, O. Andersson, V. P. Zhdanov, M. Liebi, K. Moth-Poulsen, C. Müller, C. Langhammer, *ACS Appl. Nano Mater.* **2020**, *3*, 8438.
[93] M. Matuschek, D. P. Singh, H-Ho Jeong, M. Nesterov, T. Weiss, P. Fischer, F. Neubrech, Na Liu, *Small* **2018**, *14*, 1702990.
[94] H. M. Luong, M. T. Pham, T. Guin, R. P. Madhogaria, M.-H. Phan, G. K. Larsen, T. D. Nguyen, *Nat. Commun.* **2021**, *12*, 2414.
[95] K. Sugawa, H. Tahara, A. Yamashita, J. Otsuki, T. Sagara, T. Harumoto, S. Yanagida, *ACS Nano* **2015**, *9*, 1895.
[96] S. De Marchi, S. Nunez-Sanchez, G. Bodelon, J. Perez-Juste, I. Pastoriza-Santos, *Nanoscale* **2020**, *12*, 234243.
[97] E. M. Larsson, M. E. M. Edvardsson, C. Langhammer, I. Zorić, B. Kasemo, *Rev. Sci. Instrum.* **2009**, *80*, 125105.
[98] M. A Poyli, V. M. Silkin, I. P. Chernov, P. M. Echenique, R. D Muiño, J. Aizpurua, *J. Phys. Chem. Lett.* **2012**, *3*, 2556.
[99] R. B. Schwarz, A. G. Khachaturyan, *Acta Mater.* **2006**, *54*, 313.
[100] T. B. Flanagan, W. A. Oates, *Annu. Rev. Mater. Sci.* **1991**, *21*, 269.
[101] F. D. Manchester, A. San-Martin, J. M. Pitre, *J. Phase Equilib.* **1994**, *15*, 62.
[102] S. A. Chowdhury, R. Correia, D. Francis, S. J. Brooks, B. J. S. Jones, A. W. J. Thompson, J. Hodgkinson, R. P. Tatam, *J. Lightwave Technol.* **2015**, *33*, 2535.
[103] S.-J. Huang, M. P. Mose, S. Kannaiyan, *J. Compos. Sci.* **2021**, *5*, 145.
[104] Z. Liu, J. Zhong, H. Leng, G. Xia, X. Yu, *Int. J. Hydrogen Energy* **2021**, *46*, 189880.
[105] S. Ogura, K. Fukutani, *J. Phys. Chem. C* **2017**, *121*, 3373.
[106] S. Ogura, M. Okada, K. Fukutani, *J. Phys. Chem. C* **2013**, *117*, 9366.
[107] K. D. Gilroy, A. Sundar, M. Hajfathalian, A. Yaghoubzade, T. Tan, D. Sil, E. Borguet, R. A. Hughes, S. Neretina, *Nanoscale* **2015**, *7*, 6827.

[108] Y.-W. Ma, L.-H. Zhang, Z.-W. Wu, M.-F. Yi, J. Zhang, G.-S. Jian, *Plasmonics* **2015**, *10*, 1791.
[109] E. Kretschmann, H. Raether, *Z. Naturforsch. A* **1968**, *23*, 2135.
[110] T. W. Ebbesen, H. J. Lezec, H. F. Ghaemi, T. Thio, P. A. Wolff, *Nature* **1998**, *391*, 667.
[111] W. L. Barnes, *J. Opt. A: Pure Appl. Opt.* **2006**, *8*, S87.
[112] B. Ai, H. Möhwald, D. Wang, G. Zhang, *Adv. Mater. Interfaces* **2017**, *4*, 1600271.
[113] B. Ai, Y. Zhao, *Nanophotonics* **2019**, *8*, 1.
[114] L. Bradley, D. Ye, H. M. Luong, Y. Zhao, *Nanotechnology* **2020**, *31*, 205301.
[115] B. Ai, Y. Yu, H. Möhwald, L. Wang, G. Zhang, *ACS Nano* **2014**, *8*, 1566.
[116] B. Ai, Y. Yu, H. Möhwald, G. Zhang, *Adv. Opt. Mater.* **2013**, *1*, 724.
[117] Z. Zhou, Z. Zhao, Y. Yu, B. Ai, H. Möhwald, R. C. Chiechi, J. K. W. Yang, G. Zhang, *Adv. Mater.* **2016**, *28*, 2956.
[118] Y. He, Y. Zhao, *Phys. Chem. Chem. Phys.* **2009**, *11*, 255.
[119] Y. He, Y. Zhao, *Nanotechnology* **2009**, *20*, 204008.
[120] S. Banrejee, A. Kumar, P. Ruz, V. Sudarsan, *Int. J. Energy Res.* **2021**, *45*, 175978.
[121] J. Huot, G. Liang, S. Boily, A. Van Neste, R. Schulz, *J. Alloys Compd.* **1999**, *293–295*, 495.
[122] C. Shangguan, M. Dong, G. Ren, L. Lu, B. Y. Zhang, Q. Ma, K. Xu, Y. Hu, T. Alkathiri, R. You, C. F. Mcconville, L. Zhu, J. Z. Ou, *Sens. Actuators, B* **2021**, *349*, 130740.
[123] M. W. Khan, B. Y. Zhang, K. Xu, M. Mohiuddin, A. Jannat, F. Haque, T. Alkathiri, N. Pillai, Y. Wang, S. Z. Reza, J. Li, X. Mulet, R. Babarao, N. Mahmood, J. Z. Ou, *J. Colloid Interface Sci.* **2021**, *588*, 305.
[124] B. Y. Zhang, P. Yin, Y. Hu, C. Szydzik, M. W. Khan, K. Xu, P. Thurgood, N. Mahmood, C. Dekiwadia, S. Afrin, Y. Yang, Q. Ma, C. F. Mcconville, K. Khoshmanesh, A. Mitchell, B. Hu, S. Baratchi, J. Z. Ou, *Biosens. Bioelectron.* **2022**, *198*, 113814.

Bin Ai received his B.Sc. degree in chemistry from Jilin University in 2011. Then he joined Prof. Gang Zhang's group at State Key Laboratory of Supramolecular Structure and Materials, Jilin University. In 2016, he received a Ph.D. degree in polymeric chemistry and physics. He continues his research as a postdoc at the Department of Physics and Astronomy at the University of Georgia and Department of Aerospace Engineering at Texas A&M University. Now, he is a professor at ChongQing University, China. His current scientific interests are plasmonic hydrogen sensors, nanofabrication, and intelligent information processing.

Yiping Zhao received his B.S. degree in Electronics from Peking University in 1991, and MS degree in condensed matter physics from Institute of Semiconductors, Chinese Academy of Sciences in 1994. He completed his Ph.D. degree in Physics at Rensselaer Polytechnic Institute in 1999. He is currently a Professor at the Department of Physics and Astronomy at University of Georgia. His major research interests are nanostructures and thin films fabrication and characterization, plasmonic nanostructures, chemical and biological sensors, hydrogen storage materials, nanophotocatalysts, and nanomotors.